Universidade de São Paulo
Instituto de Astronomia, Geofísica e Ciências Atmosféricas
Departamento de Astronomia

Artur Vemado

Radiative cooling and state transitions in stellar mass black holes

São Paulo
2020

Artur Vemado

Radiative cooling and state transitions in stellar mass black holes

Dissertation presented to the Astronomy department of the Institute of Astronomy, Geophysics and Atmospheric Sciences of the University of São Paulo as partial requisite to obtain the Master in Sciences title.

Concentration Area: Astronomy
Advisor: Prof. Dr. Rodrigo Nemmen

Corrected Version. The original is available in IAG-USP

São Paulo
2020

To Letícia and Ringo...

Acknowledgements

This work was possible only because of the great support of my girlfriend Letícia and my dog Ringo. Without them I would not be able to finish this work. Thus, here is my special thanks to them.

I would like to pay my special regards to my parents Antonia and João Ricardo that gave me all the support for getting where I am. I would also like to thank Guilherme, Felipe, Lorena, Mariana and Otávio for the great moments I spent with them that made my life better.

I wish to show my gratitude to my supervisor Rodrigo Nemmen for giving me the greatest advises and leading me through this scientific journey.

I would like to thank my friends from the Black Hole group and the friends I made at USP for making the graduate life happier.

I would like to thank all the people that I met in my journey through life that made my life a little better.

I would like to acknowledge the clusters Santos Dumont and Águia for giving me the support I needed for the simulations.

I would like to express my sincere gratitude to the support given by grant 2017/25710-1 and 2017/01461-2, São Paulo Research Foundation (FAPESP). Also, this study was financed in part by the Coordenação de Aperfeiçoamento de Pessoal de Nível Superior - Brasil (CAPES) - Finance Code 001.

I would like to express my sincere gratitude for all the staff from IAG-USP.

"*If I have seen further it is by standing on the shoulders of Giants*"

Sir Isaac Newton

"*We live in a society exquisitely dependent on science and technology, in which hardly anyone knows anything about science and technology*"

Carl Sagan

Resumo

Binárias de buracos negros em raio X são conhecidas por apresentarem diferentes estados espectrais ao longo de suas vidas. Esses estados podem ser explicadas pela presença de um disco quente e geometricamente espesso para o estado duro e um disco mais frio e fino para o estado mole. Entretanto, o grau em que a corona quente a o disco fino coexistem não é bem entendido. Em particular, não é claro como o disco interno do disco fino e as propriedades da corona (e.g. tamanho e temperatura) estão relacionadas às propriedades fundamental do sistema como a taxa de acreção do buraco negro $\dot{M}$. Neste trabalho, simulações hidrodinâmicas de discos de acreção ao redor de buracos negros estelares com resfriamento radiativo em duas dimensões foram realizadas para investigar a interação entre o disco fino e a corona quente e a relação entre o raio de truncamento $R_{\rm tr}$ e $\dot{M}$. As contribuições de processos de resfriamento como Bremsstrahlung, síncrotron e síncrotron comptonizado foram incorporados na equação de energia. Os principais resultados deste trabalho são (i) a nova relação $R_{\rm tr} \propto \dot{m}^{-1/2}$ conectando as duas propriedades básicas de buracos negros acretando e (ii) a diminuição da temperatura e da extensão espacial da corona com o aumento de $\dot{M}$. Espera-se que estes resultados lancem luz sobre as observações de binárias de buracos negros.

Abstract

Black hole (BH) X-ray binaries are characterized by different spectral states along their lives. These states can be explained by the presence of a hot, geometrically thick corona for the hard state and a colder thin disk for the soft state. However, the degree to which the hot corona and the thin accretion disk coexist is not well understood. In particular, it is unclear how the inner radius of the thin disk and the properties of the hot corona (e.g. size and temperature) are related to the fundamental system properties such as the BH mass accretion rate $\dot{M}$. In this work, two-dimensional hydrodynamical simulations with radiative cooling of accretion flows around stellar black holes were performed to investigate the interplay between the thin disk and hot corona and the relation between the truncation radius $R_{\rm tr}$ and $\dot{M}$. The contribution of Bremsstrahlung, synchrotron and comptonized synchrotron cooling processes were incorporated in the energy equation. The main results of this work are (i) the new relation $R_{\rm tr} \propto \dot{m}^{-1/2}$ connecting two basic properties of accreting BHs and (ii) the decrease of both temperature and spatial extent of the corona with increasing $\dot{M}$. These results are expected to shed light on observations of BH binaries.

List of Figures

List of Tables

Contents

Chapter 1

Introduction

Black holes (BHs) are regions of the spacetime where gravitational potential wells are so deep that not even light can escape from it. They are not only expected from general relativity (GR), but actually exist in nature (Frolov and Novikov, 1998). Within the last decades, with the improvement in the observational astronomy, BHs have called a lot of attention due to their impressive effects in the universe. They are associated with very powerful astrophysical events such as gamma-ray bursts, active galactic nuclei (AGN), supernovas, X-ray binary systems, and others (Meier, 2012). Some of the most recent events associated with BHs are the gravitational waves detected by LIGO collaboration (Abbott et al., 2016), which opened a whole new era for astrophysics of BH. The investigation of these events are essential to understand BHs, gravity, and the universe itself.

The most simple solution to a BH is the Schwarzschild solution, which are BHs that have no rotation and which radius can be defined as $R_{\rm S} = 2GM/c^2$, where G is the gravitational constant, M is the mass of the BH and c is the speed of light. Using this solution, the only parameter that matters for a BH is its mass, but in the real universe their rotation can be described by the spin parameter $a \equiv J/Mc$, where J is the angular momentum of the BH and Mc is the maximum angular momentum permitted. Thus, for describing a BH the main parameters are: mass and spin (Hartle, 2003). There are some solutions that consider the charge of the BH (Newman et al., 1965), but we do not take it into account because the surrounding plasma would rapidly neutralize its charge.

There are two categories of BHs: the supermassive (SMBH) and stellar mass ones. While SMBHs have masses of more than ten millions of solar masses, a stellar BH usually has a mass of five to several tens of solar masses. Between these two mass ranges we can find the intermediate mass BHs. However, until today there is no firm observational proof

of their existence (Greene et al., 2019). The focus of this work is on stellar mass BHs in binary systems.

The strongest evidence for the existence of stellar BHs come from observations of X-ray binary systems. Dynamical measurements of the orbit indicate the presence of massive objects with masses above $\approx 2M_{\odot}$ which is the maximum mass for a neutron star, but there is no evidence for emission from a solid surface (e.g Ozel et al., 2012). The pioneer candidate BH X-ray binary (BHB) system detected was Cygnus X-1 (Bowyer et al., 1965). After confirming that the object in question was indeed a BHB system, astronomers discovered many tens of them in the Milky Way and throughout the local universe (McClintock and Remillard, 2009).

BHBs are complex systems with variability timescales ranging from months to many years. They are essential targets for astronomy since they are laboratories for learning more about the BH accretion and its effects. It is likely that the behavior of stellar BHs scales up to SMBHs in AGNs (Merloni et al., 2003; Fender and Belloni, 2012; Nemmen et al., 2012). In fact, there are some authors that propose that the bright AGN are analogy to BHBs in the soft state, while low-luminosity AGN are correspondent to BHBs in the hard state (Ho, 2008; Antonucci, 2012; Done, 2014). If this is the case, it could also be a laboratory for us to understand the growth of galaxies, because while SMBHs—which are encountered in most, if not in all, galaxies—have very large timescales, BHBs have humanly accessible ones, and it is known that SMBHs play a crucial role in their galaxies' evolution by releasing energy. This released energy may have the effect of quenching the star formation by heating or ejecting the material of the galaxy (Cattaneo et al., 2009). Thus, it would be possible to extrapolate the results to SMBHs and, therefore, to study galaxy evolution.

Over time, these systems display different spectral features (cf. section 1.2) corresponding to distinct states. The issue here is how and why these features change with time. What is the physics behind the state transitions of the accretion flow? One appealing possibility is that the state transitions are related to the temporal evolution of radiative cooling in the disk.

1.1 Accretion physics

Because of angular momentum conservation, the matter that falls into the BH will form a disk-like structure. For this matter to be accreted by the BH we need a dissipation mechanism that removes angular momentum from the flow. Magnetic forces in an ionized plasma are the favored mechanism that supplies this friction, efficiently transporting angular momentum outwards and allowing accretion to proceed (Balbus and Hawley, 1998).

This accretion process also converts some of the gravitational energy into heat and can release part of its rest mass, providing the main power source of AGNs, BHBs and gamma-ray bursts (Meier, 2012). An accretion flow is characterized primarily by the efficiency of the conversion of rest-mass energy associated with the accreting matter into radiation: $\epsilon = L/\dot{M}c^2$ where L is the luminosity produced by the accretion flow and $\dot{M}$ is the mass accretion rate of the BH, which means that $\dot{M}c^2$ is the rate at which energy is accreted onto the BH.

The geometry and dynamics of the accretion flow is sensitive to this efficiency, which is commonly parameterized in terms of the accretion rate in Eddington units $\dot{m} \equiv \dot{M}/\dot{M}_{\rm Edd}$ where $\dot{M}_{\rm Edd} \equiv 4\pi GMm_{\rm p}/(\eta c\sigma_{\rm T})$ is the Eddington accretion rate, M is the mass of the BH, $m_{\rm p}$ is the proton mass, $\sigma_{\rm T}$ is the Thompson cross section and η is usually fixed at 0.1 (Frank et al., 2002). Thus, based on the radiative efficiency and the value of $\dot{m}$ we can divide the accretion flow into three main different types:

Radiatively inefficient accretion flow at low $\dot{m}$: Due to the low densities, meaning low $\dot{M}$—more precisely, $\dot{m} \lesssim 0.01$—the gas cannot radiate its thermal energy efficiently and becomes extremely hot ($T \sim 10^{10-12}$ K). This causes the accretion flow to puff up, becoming geometrically thick ($H \sim R$, where H is the scale height of the accretion flow) and optically thin with $\epsilon \ll 1$ (Nemmen et al., 2014; Yuan and Narayan, 2014). From now on we will refer to this kind of accretion a RIAF.

Thin Accretion disks: At higher densities, which means moderately high accretion rate ($0.01 \lesssim \dot{m} \lesssim 1$) the cooling time is shorter than the accretion time scale. Thus, the gas cools efficiently (usually $\epsilon \sim 0.1$), becomes cold and collapses into a geometrically thin accretion disk ($H \ll R$; Shakura and Sunyaev, 1973; Nemmen and Brotherton, 2010).

RIAF at high $\dot{m}$: because of the high densities associated with super-Eddington accretion rates ($\dot{m} \gtrsim 1$), the gas is optically thick and the radiation gets trapped in the gas, not being able to radiate. Thus, the flow gets very hot and becomes geometrically thick (Abramowicz et al., 1998). This kind of accretion flow is out of the scope of this work because our work does not include radiation pressure, which is very important in this regime.

In Figure 1.1 the different states of the accretion flow as a function of $\dot{m}$ are illustrated. In this cartoon, the high-$\dot{M}$ RIAF is not shown. As mentioned before, it is possible to see that the so called "High State" corresponds to the thin accretion disk while the "Low State" as well as the "Quiescent State" correspond to the RIAF state at low accretion rates.

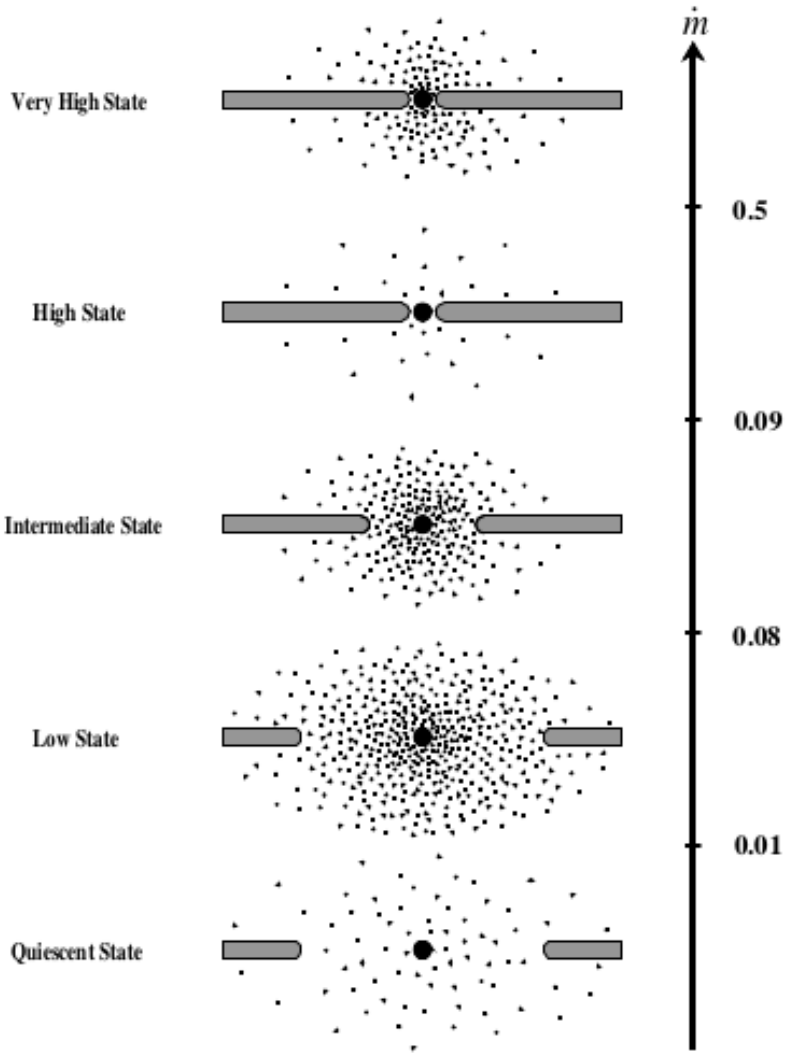

Figure 1.1: The different states of BH accretion around stellar mass BHs with the corresponding accretion rates in Eddington units. Image taken from Narayan et al. (1998).

1.2 State transition in BHBs

BHBs are systems where a BH is fed by a companion star with a mass of about $1M_{\odot}$ (Figure 1.2). The mass transfer occurs through the L1 point in the Roche Lobe, which is the gravitational equipotential surface found in the solution of a restricted three-body problem (Figure 1.3).

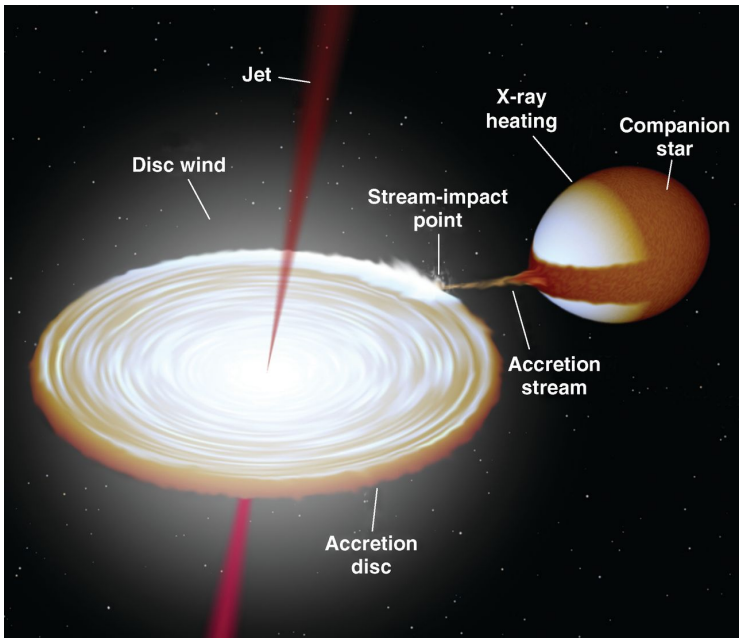

Figure 1.2: Artistic impression of a BHB. The components of the system are based on the system GX 339-4. Image taken from Fender and Belloni (2012).

Now that the main kinds of accretion flows have been presented, it is possible to discuss the main subject of this work: black hole binaries. These systems are known to be characterized by at least two distinct states characterized by dramatically different spectral and timing properties (e.g. Remillard and McClintock 2006; Fender and Belloni 2012).

Generally, as the source enters its outburst it goes through the so-called *hard state* which is lower in luminosity and has a hard power-law spectrum. The thermal component is suppressed and the accretion flow is explained as a RIAF. As the system gets more luminous it enters the *soft state*, in which the spectrum is now dominated by a thermal component. This multiblackbody spectrum can be explained as a thin accretion disk. During the transition there is a state where both the hard and soft components are comparable: the *intermediate state*.

The BHB states can be understood in the context of the widely accepted truncated

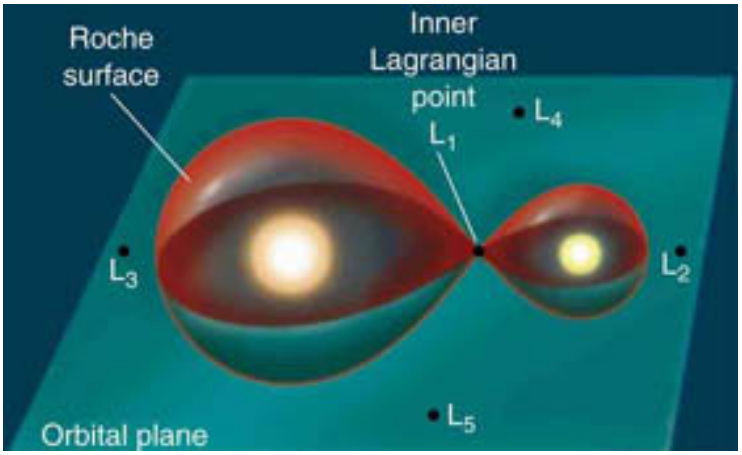

Figure 1.3: Example of the Roche lobe in a binary system, where the Lagrangian points are displayed. The most important point is L1 at which the BH accretes matter from the companion. Credit: https://www.daviddarling.info/encyclopedia/R/Roche_lobe.html, accessed on January 6$^{\text{th}}$ 2020.

accretion-jet model (Esin et al., 1997; Yuan et al., 2005; Plant et al., 2014; Ingram and Done, 2011). In this model, the thin accretion disk is believed to be truncated at certain truncation radius R_{tr} inside of which it transitions into a RIAF. There is also a jet component launched when the system is in hard or intermediate state.

Figure 1.4 shows the evolution of a BHB as it evolves and goes through each state, with the different components: disk, jet and wind. Before the outburst the sources are in quiescence state and because of that they are rarely monitored, so the first thing detected is an increase of the luminosity of the system (A $\longrightarrow$ B). This happens because initially the accretion rate of the BH is lower than the mass transfer from the companion star, which means that the accretion flow starts getting denser and, consequently, the accretion rate increases. That increase of accretion rate causes an increase in the luminosity. Meanwhile, the thin accretion disk starts getting closer to the BH and the thermal spectra becomes important (B $\longrightarrow$ C). The intermediate state has been reached.

As the truncation radius decreases, the thermal component becomes dominant and the system transitions to the soft state (C $\longrightarrow$ D). Now, with the dense and thin accretion disk very close to the BH ($R_{tr} \sim R_{ISCO}$, where R_{ISCO} is the innermost stable circular orbit) the accretion rate is greater than the mass transfer and the total mass of the disk starts dropping. As the gas gets accreted the inner parts of the thin accretion disk become less dense and the cooling time becomes bigger than the viscous time (Narayan and Yi, 1995;

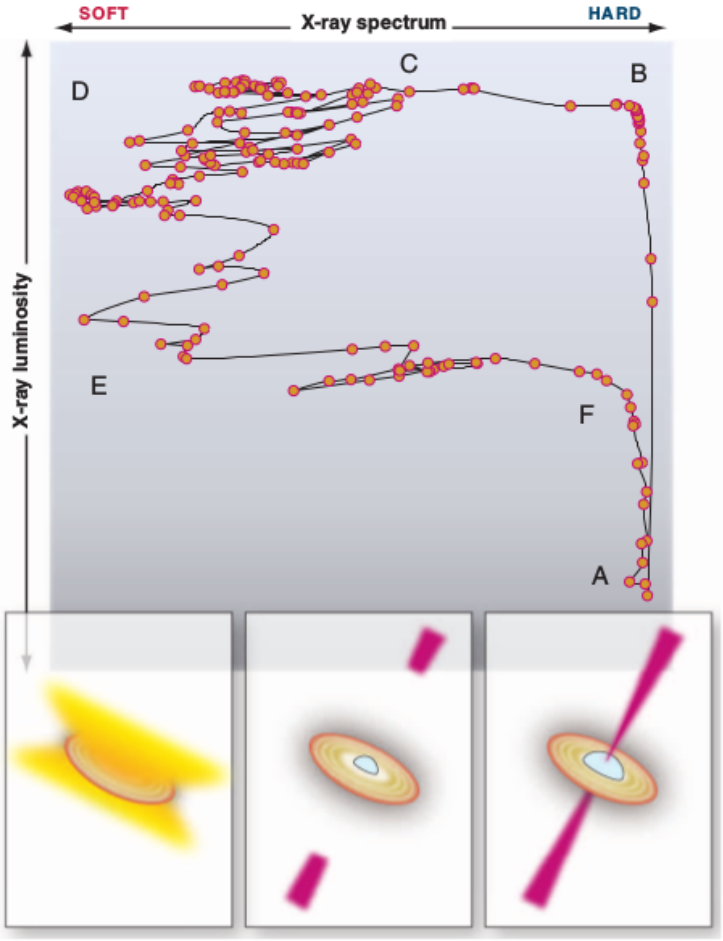

Figure 1.4: Hardness-intensity diagram for a BHB. The horizontal axis represents the X-ray hardness and the vertical one is the X-ray luminosity. The observations correspond to GX 339-4. Credit: Fender and Belloni (2012).

Yuan and Narayan, 2014), so the gas becomes hotter and puffs up into a hot, geometrically thick and optically thin corona (i.e. the RIAF). Thus, the accretion rate drops along with an increase of R_{tr}, which means a drop in luminosity until it transitions back to the hard state and the cycle begins again (D $\longrightarrow$ E $\longrightarrow$ F $\longrightarrow$ A).

Different features are observed along with each part of the cycle. In the hard state (A $\longrightarrow$ B), it is seen that the characteristic time scales of quasi-periodic oscillations (QPOs) decrease and the jets appear. In the transition (B $\longrightarrow$ D), the characteristic frequencies of variability rises until it is replaced by a single QPO. The jet, on the other hand, starts disappearing. In the soft state (D $\longrightarrow$ E) the QPOs disappear and the jets fade away. Finally, in the return to the quiescent state (E $\longrightarrow$ F) the jet reappear and the characteristic time scale of variability starts rising. A more detailed description of the observational

characteristics of BHBs can be found in Fender and Belloni (2012)

The main purpose of this work is to study the dependence of the truncation radius on the mass accretion rate and the dynamics of a two phase disk (RIAF + thin disk). In order to address this, hydrodynamical simulations were performed, implementing radiative cooling including the relevant processes for BHBs (breemstrahlung, synchrotron and comptonized synchrotron) by adding extra terms to the energy equation, so that it would be possible to calculate the energy loss due to these cooling processes, which plays a major role in truncating the disk.

This work is organized as follows: in Chapter 2, the methods and equations for the HD simulations will be described, as well as the implementation of the radiative cooling. In Chapter 3 the results from the analysis of the simulations will be presented. In Chapter 4 the results and the caveats of the simulations will be discussed. Finally, in Chapter 5 all results will be summarized and future perspectives will be presented.

Chapter 2

Methods

In this work, numerical simulation of accretion flows will be performed following the prescription of Papaloizou and Pringle (1984) (cf. section 2.4), where the flow is initially a torus in order to mimic the RIAF state. The implementation of energy loss via breemstrahlung, synchrotron and Comptonized synchrotron cooling is described as well.

The summary of this chapter is as follows. The basic equations of hydrodynamics and the numerical solver will be presented in sections 2.1 and 2.2. An approximation for the cooling will be presented in section 2.3. The pseudo-Newtonian potential of Paczynsky and Wiita (1980) (cf. section 2.1) will be used. This is a good approximation to a Schwarzschild BH. Since our simulations are purely hydrodynamical (HD)—i.e. there will be no magnetic fields—the magnetorotational instability (MRI; Balbus and Hawley, 1998) which is responsible for the energy and angular momentum dissipation will be incorporated by an appropriate viscous stress tensor prescription (section 2.4).

2.1 Equations of hydrodynamics

For this work, the code `PLUTO` is adopted which solves the equations of fluid dynamics in spherical coordinates (R, θ, ϕ):

$$\frac{d\rho}{dt} + \rho\nabla\cdot\boldsymbol{v} = 0, \tag{2.1}$$

$$\rho\frac{d\boldsymbol{v}}{dt} = -\nabla P_{\rm tot} - \rho\nabla\phi + \nabla\cdot\boldsymbol{T}, \tag{2.2}$$

$$\rho\frac{d(e/\rho)}{dt} = -P_{\rm gas}\nabla\cdot\boldsymbol{v} + \boldsymbol{T}^2/\mu - Q^-_{\rm rad}. \tag{2.3}$$

Here, ρ is the mass density, $\boldsymbol{v}$ is the gas velocity, $P_{\rm tot} \equiv P_{\rm gas} + P_{\rm mag}$ is the total pressure (gas + magnetic), e is the internal energy density, $\boldsymbol{T}$ is the viscous stress tensor, and

$$\phi = -\frac{GM}{R - R_{\rm s}} \tag{2.4}$$

is the pseudo-Newtonian gravitational potential adopted in the simulations (Paczynsky and Wiita, 1980). The radiative cooling rate $Q^{-}_{\rm rad}$ is incorporated in the energy equation 2.3. This will be described in more details in section 2.3.

Magnetohydrodynamical turbulence driven by MRI is expected in accretion flow simulations (Balbus and Hawley, 1998; Porth et al., 2019; Stone and Pringle, 2001). In this case, the simulations are purely HD. A simpler approach to incorporate angular momentum dissipation is adopted: the α-viscosity of Shakura and Sunyaev (1973). Concretely, this consists of taking into account a non-zero azimuthal component of T is included, following Stone et al. (1999):

$$T_{r\phi} = \mu R \frac{\partial}{\partial R}\left(\frac{v_\phi}{R}\right), \tag{2.5}$$

$$T_{\theta\phi} = \frac{\mu \sin\theta}{R}\frac{\partial}{\partial \theta}\left(\frac{v_\phi}{\sin\theta}\right). \tag{2.6}$$

Here, $\mu = \nu\rho$ is the viscosity coefficient and ν is the kinematic viscosity coefficient.

In this work, the prescription used for the kinematic coefficient is the "K-model"in Stone et al. (1999), which corresponds to $\nu = \alpha r^{1/2}$ where α is a constant similar to the standard α-prescription of Shakura and Sunyaev (1973). Here, $\alpha = 0.01$ is set which is a common and well discussed choice (Wu et al., 2016; Das and Sharma, 2013).

2.2 PLUTO

2.2.1 Numerical methods

All simulations were done using the code PLUTO (Mignone et al., 2007). PLUTO is a finite-volume, shock-capturing code designed to integrate the system of conservation laws

$$\frac{\partial \boldsymbol{U}}{\partial t} = -\nabla \cdot T(\boldsymbol{U}) + S(\boldsymbol{U}), \tag{2.7}$$

where $\boldsymbol{U}$ encompass the conservative quantities, $T(\boldsymbol{U})$ is a rank-2 tensor representing the flux of the quantities and $S(\boldsymbol{U})$ represents the source terms, such as gravity and the radiative cooling rate.

The components of $\boldsymbol{U}$ are the primary variables that will be updated. The fluxes are more easily computed using a different set of primitive variables contained in the primitive vector $\boldsymbol{V} = (\rho, \boldsymbol{v}, p)^T$, where p is the pressure. The transformation $\boldsymbol{U} \rightarrow \boldsymbol{V}$ is beneficial because the interpolation on the primitive variables enforces physical constraints as pressure positivity and sub-luminal speed in the relativistic case. Besides that, as the flux is more easily computed using $\boldsymbol{V}$, the Riemann problem will be facilitated.

Figure 2.1 summarizes the steps taken by PLUTO, which are also listed below (e.g. Toro 2013):

1. The conversion from conserved variables into primitive ones;
2. The values of primitive variables are computed at the edges of the cells;
3. The Riemann problem is solved using one of the Riemann Solvers available in the code (for the simulations in this work, *hll* will be used; see Toro et al., 1994; Batten et al., 1997, for HD equations);
4. A new temporal state is calculated

.

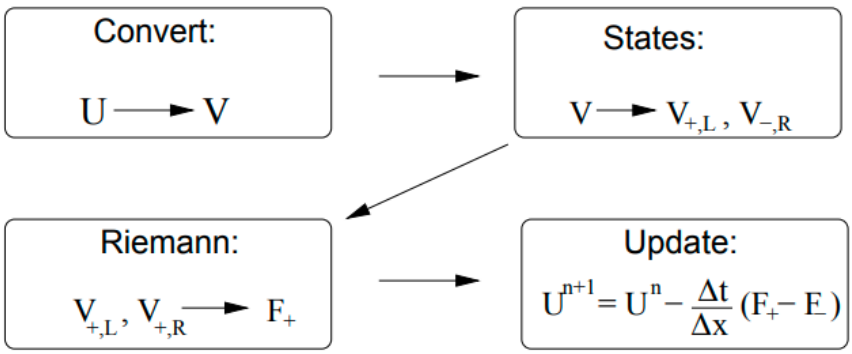

Figure 2.1: Flowchart of the conversion of $\boldsymbol{U}$ to $\boldsymbol{V}$ in PLUTO. Image taken from Mignone et al. (2007).

PLUTO uses a Godunov-type scheme to solve the hyperbolic systems of partial differential equations [1]. This method is a conservative finite-volume method which solves the exact or approximate Riemann problems at each inter-cell boundary. Riemann problem shows

[1] The equations of hydrodynamics are hyperbolic (Toro, 2013).

up naturally in the finite volume method when solving conservation laws such as equation 2.7, due to the discretization of the grid.

For simplicity, the Godunov scheme will be presented in only one dimension and without including the source terms; it can easily be extended to higher dimensions and the implementation of the source terms is trivial. Figure 2.2 shows a one dimensional grid which will be used to present the Godunov method.

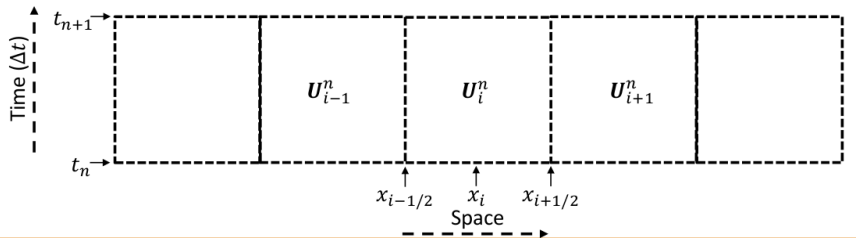

Figure 2.2: One dimensional grid illustrating the derivation of the Godunov method. Image taken from https://numericalastrophysics.files.wordpress.com/2018/08/cap5-godunov.pdf (lecture notes for numerical astrophysics course, IAG USP).

The exact expression of the Godunov scheme is given by

$$\boldsymbol{U}_i^{n+1} = \boldsymbol{U}_i^n + \frac{\Delta t}{\Delta x}\left(\boldsymbol{F}_{i-1/2} - \boldsymbol{F}_{i+1/2}\right), \tag{2.8}$$

where $\boldsymbol{F}_{i\pm1/2}$ is the flux between cells. To compute this flux, a Riemann solver is needed.

Another method is needed to solve for the time step. Here, the 3$^{\text{rd}}$-order Runge-Kutta method was used. For this method, the increment between two consecutive steps in time, $\Delta t^n = t^{n+1} - t^n$, needs to be calculated. Using $\boldsymbol{L}$ as the discrete spatial operator (right hand side of Eq. 2.7), $\boldsymbol{U}^{n+1}$ is given by

$$\begin{aligned}
\boldsymbol{U}^* &= \boldsymbol{U}^n + \Delta t^n \boldsymbol{L}(\boldsymbol{U}^n), \\
\boldsymbol{U}^{**} &= \frac{1}{4}(3\boldsymbol{U}^n + \boldsymbol{U}^* + \Delta t^n \boldsymbol{L}(\boldsymbol{U}^*)), \\
\boldsymbol{U}^{n+1} &= \frac{1}{3}(\boldsymbol{U}^n + 2\boldsymbol{U}^{**} + 2\Delta t^n \boldsymbol{L}(\boldsymbol{U}^{**})).
\end{aligned} \tag{2.9}$$

2.2.2 Hydrodynamical module

For the HD module used in this work, PLUTO solves the equations (2.1)-(2.3) which can be formulated as

$$\frac{\partial}{\partial t}\begin{pmatrix}\rho\\ \boldsymbol{m}\\ E+\rho\Phi\end{pmatrix}+\nabla\cdot\begin{pmatrix}\rho\boldsymbol{v}\\ \boldsymbol{m}\boldsymbol{v}+p\boldsymbol{I}\\ (E+p+\rho\Phi)\boldsymbol{v}\end{pmatrix}^{T}=\begin{pmatrix}0\\ -\rho\nabla\Phi+\rho\boldsymbol{g}\\ \boldsymbol{m}\cdot\boldsymbol{g}\end{pmatrix} \tag{2.10}$$

where $\boldsymbol{m}=\rho\boldsymbol{v}$ is the momentum density, $E=\rho e+\boldsymbol{m}^2/2\rho$ is the total energy and $\boldsymbol{I}$ is the unit tensor. Two source terms need to be added to the right hand side of this equation: the viscous stress tensor—which incorporates the angular momentum removal through the α-viscosity—and the radiative cooling rate—which include the energy losses due to radiation.

The viscous stress tensor $\boldsymbol{T}$ is added as $\nabla\cdot\boldsymbol{T}$. The radiative cooling rate will be described in the next subsection.

2.2.3 Radiative cooling rate module

The cooling module of PLUTO allows the inclusion of time-dependent optically thin radiative losses. This means that radiation pressure will not be considered in the momentum equation such as in Sadowski et al. (2014), McKinney et al. (2014) and Ryan et al. (2015). In addition, radiation transfer will not be taken into account into detail. Instead, it will be incorporated in an approximated, first-order fashion.

This is implemented following a fractional step formalism in which the hydrodynamical evolution and the source step are solved separately using operator splitting. This splitting method separates the original equation into two parts over a time step, computes them separately and then combines them to yield one solution to the original equation (Glowinski et al., 2016, Chapter 3). Thus, PLUTO solves the internal energy equation

$$\frac{\partial(\rho e)}{\partial t}=-Q^{-}_{\rm rad}(n_e,R,T_e) \tag{2.11}$$

where R is the distance from the BH, T_e is the electron temperature and $n_e=\rho/\mu_{\rm e}/m_{\rm u}$ is the electron number density, where $\mu_{\rm e}=1.14$ and $m_{\rm u}$ is the atomic mass unit. In fact, in the original PLUTO code it was not possible to implement a distance dependent cooling rate because of how the code was structured. It was necessary to make some important changes

to the radiative cooling portion of the code. This required some time for implementation and successful testing.

The method used to compute equation 2.11 was the standard one, as will be explained below. Firstly, a collection of values for $Q^{-}_{\rm rad}(n_e, R, T_e)$ were precalculated (cf. section 2.3 for the approximations used) using a range of values for each parameter: $10^{11} \leq n_e/{\rm cm}^{-3} \leq 10^{20}$, $1.3R_{\rm s} \leq R \leq 400R_{\rm s}$ and $10^6 \leq T_e/K \leq 10^{12}$ which are typical values for the accretion flows in BHBs. For each parameter, 100 values were generated thereby producing a table with 10^6 values of cooling rate in units of erg s^{-1} cm^{-3}. These values were equally spaced in the log space. Secondly, it was necessary to write codes that generate a lookup table with the radiative cooling rates tabulated as a function of n_e, R and T_e. The lookup-table approach is faster than computing $Q^{-}_{\rm rad}$ on-the-fly during the HD simulations. Finally, a linear interpolation was used to get the values of $Q^{-}_{\rm rad}$ in points of the parameter of space in-between tabulated values. By doing this, the code is able to solve equation 2.11 and advance to the next time steps of the simulations.

An important point to stress here is that both the radiative cooling and viscosity are only taken into account within the accretion flow. In order to do that, a tracer variable available in `PLUTO` is used which tracks the region occupied by the accretion flow. Using the tracer variable, it is possible to distinguish the accretion flow from the low-density artificial atmosphere. Basically, this variable is set to ~ 1 in the accretion flow and $\ll 1$ in the rest of the domain.

2.3 Radiative cooling equation

Due to the difference in mass between ions and electron, the gas cooling occurs primarily via electrons through a variety of processes. Here, the main radiative cooling processes that take place in hot accretion flows are incorporated following Narayan and Yi (1995).

The total radiative cooling rate will be expressed as

$$Q^{-}_{rad} = Q^{-}_{brem} + Q^{-}_{syn} + Q^{-}_{ssc} \tag{2.12}$$

where Q^{-}_{brem} is the bremsstrahlung emission including both the electron-ion and electron-electron interactions, Q^{-}_{syn} is the optically thin synchrotron emission and Q^{-}_{ssc} is the radiative cooling due to the comptonized synchrotron emission.

2.3.1 Bremsstrahlung

The bremsstrahlung emission is given by Narayan and Yi (1995) as

$$Q^{-}_{brem} = Q^{-}_{ei} + Q^{-}_{ee} \tag{2.13}$$

where the subscript ei and ee denote the electron-ion and the electron-electron rates. Here, the final equations were derived by Stepney and Guilbert (1983). For the formulas of electron-ion breemstrahlung, it is assumed that the temperature of the protons is small enough to neglect its motion and the electrons follow a Maxwellian energy distribution. The spectral emissivity is integrated and the fit results in the following equations

$$Q^{-}_{ei} = 1.48 \times 10^{-22} n_e^2 \times F(\theta_e), \tag{2.14}$$

which is given in units of erg cm^{-3} s^{-1}, where $F(\theta_e)$ is given by different expressions depending on the value of $\theta_e \equiv kT_e/m_e c^2$:

$$F(\theta_e) = \begin{cases} \frac{9\theta_e}{2\pi}\left[\ln\left(1.123\theta_e + 0.48\right) + 1.5\right] & \text{if } \theta_e < 1, \\ 4\left(\frac{2\theta_e}{\pi^3}\right)^{1/2}\left(1 + 1.781\theta_e^{1.34}\right) & \text{if } \theta_e > 1. \end{cases}$$

For the electron-electron rate, Stepney and Guilbert (1983) gives the photon spectrum and integrate it with an approximated cross-section, resulting in the equations below.

$$Q^{-}_{ee} = \begin{cases} 2.56 \times 10^{-22} n_e^2 \theta_e^{3/2}\left(1 + 1.1\theta_e + \theta_e^2 - 1.25\theta_e^{5/2}\right) & \text{if } \theta_e < 1, \\ 3.40 \times 10^{-22} n_e^2 \theta_e \left(\ln 1.123\theta_e + 1.28\right) & \text{if } \theta_e > 1. \end{cases}$$

According to Stepney and Guilbert (1983), with all the approximations the formulas above incur in errors of less than 5 per cent. Note that there are some constants here that are different from Stepney and Guilbert (1983); these changes were implemented in Narayan and Yi (1995) to ensure smoothness across $\theta_e = 1$.

2.3.2 Synchrotron

For the derivation of the synchrotron formula, the optically thin limit is adopted according to which the spectrum of synchrotron emission is given by a relativistic Maxwellian distribution of electrons (Pacholczyk, 1970). It is assumed that the angle between the velocity vector of the electron and the direction of the local magnetic field follows an isotropic

distribution, an assumption that introduces an error of less than 2 per cent (Narayan and Yi, 1995).

In the optically thin limit of synchrotron emission, the emission is assumed to be self-absorbed below a critical frequency ν_c. ν_c is estimated by assuming that at each radius R, the synchrotron emission occurs over a volume $2 \times H \times \Delta s$ where H is the scale height and Δs is the surface area, following Wu et al. 2016. Equating the synchrotron emission to the Rayleigh-Jeans blackbody emission results in a transcendental equation for x_m given by

$$\exp\left(1.8899 x_m^{1/3}\right) = 2.49 \times 10^{-10} \frac{12\pi n_e H}{B} \frac{1}{\theta_e^3 K_2(1/\theta_e)} \left(\frac{1}{x_m^{7/6}} + \frac{0.40}{x_m^{17/12}} + \frac{0.5316}{x_m^{5/3}} \right) \tag{2.15}$$

where K_2 is the modified Bessel's function. This equation is solved at each H (i.e. each R) to obtain x_m; afterwards, it is then used to calculate ν_c from equation

$$\nu_c = \frac{3}{2} \nu_o \theta_e^2 x_m \tag{2.16}$$

where $\nu_o = 2.80 \times 10^6 B$ Hz and B is given in units of Gauss.

To obtain the cooling rate per unit volume from synchrotron radiation, the total cooling over a shell extending from R to $R+dR$ is equated with the net flux reaching an observer at infinity from this shell and assuming that at each frequency ν the observer sees a blackbody source with radius determined by the condition $\nu = \nu_c(R)$. This results in

$$Q_{syn}^{-} = \frac{2\pi}{3c^2} k T_e(R) \frac{d\nu_c^3(R)}{dR} \approx \frac{2\pi}{3c^2} k T_e(R) \frac{\nu_c^3(R)}{R}. \tag{2.17}$$

Equation 2.17 is written in a form that explicitly ensures that the integral of Q_{syn}^{-} over the entire flow is equal to the total cooling radiation that reaches infinity. It is also written in a way to simplify the computation, avoiding the derivative $d\nu_c^3(R)/dR$, which would cause the integration to be much slower.

2.3.3 Comptonization of Synchrotron Radiation

In this work the nonlocal radiative transfer effects in the optically thin mode are neglected. It is very important to take into account the scattering of the photons by hot thermal electrons, specially in the inner regions of the accretion flow.

The Compton cooling is mainly characterized by the comptonized energy enhancement factor η. This parameter is defined as the average change in energy of a photon between

injection and escape. An approximate description for η is given by Dermer et al. (1991) as

$$\eta = 1 + \frac{P(A-1)}{1-PA}\left[1 - \left(\frac{x}{3\theta_e}\right)^{-1-\frac{\ln P}{\ln A}}\right] \tag{2.18}$$

where $x \equiv \frac{h\nu}{m_e c^2}$, P is the probability of an escaping photon to be scattered,

$$P = 1 - \exp\left(-\tau_{es}\right), \tag{2.19}$$

$\tau_{es} = 2n_e\sigma_T H$ the scattering optical depth and A is the mean amplification factor in the energy of a scattered photon when the scattering electrons have a Maxwellian velocity distribution of temperature θ_e,

$$A = 1 + 4\theta_e + 16\theta_e^2. \tag{2.20}$$

In the synchrotron cooling model, the escaping radiation is emitted mostly at the local self-absorption cutoff frequency ν_c. The Comptonization of this radiation gives an additional cooling rate of

$$Q^-_{ssc} = Q^-_{syn}\left[\eta(\nu_c, \tau_{es}) - 1\right]. \tag{2.21}$$

2.3.4 Optically thick cooling

Since the interest of this work is to understand the interplay between the two possible accretion flows in BHBs—RIAF + thin disk—it is important to compute the radiative cooling of the higher density and colder regions: the thin accretion disk. Thin disks are geometrically thin and optically thick, thus they radiate like a modified, multicolor blackbody.

To take this into account, the effective surface flux from a thin disk is needed. An improved expression for the net volume cooling rate of the accreting gas of Hubeny (1990) is adopted,

$$Q^-_{rad} = \frac{4\sigma T_e^4}{H}\frac{1}{3\tau/2 + \sqrt{3} + 1/\tau_{abs}}. \tag{2.22}$$

Here, $\tau = \tau_{abs} + \tau_{es}$ is the total optical depth and τ_{abs} can be approximated as

$$\tau_{abs} = \frac{H}{4\sigma T_e^4}\left(Q^-_{brem} + Q^-_{syn} + Q^-_{ssc}\right). \tag{2.23}$$

(cf. Eq. 3.33 from Narayan and Yi 1995). Note that this expression is valid for both optically thick and thin limits, because when $\tau \gg 1$, Eq. 2.22 results in the appropriate blackbody limit. On the other hand, when $\tau \ll 1$, Eq. 2.22 becomes exactly Eq. 2.12. Thus, Eq. 2.22 is the final equation that is used to compute the radiative cooling.

2.4 Initial conditions

2.4.1 Units and grid

The units adopted are such that $G = M = 1$ and $c = \sqrt{2}$, which result in $R_\mathrm{s} = 1$. Distances in the simulations are parameterized in terms of the Schwarzschild radius. For the analysis of all simulations, $M = 10M_\odot$ was adopted which is suitable for the BHBs.

The grid used in all simulations is a logarithmic grid in R bounded by $1.3R_\mathrm{s} < R < 400R_\mathrm{s}$ and a uniform grid in θ bounded by $2^\circ < \theta < 178^\circ$. As the spin parameter a_* does not seem to be a crucial parameter to understand BHB state transitions (Remillard and McClintock, 2006) and this work is not concerned with jet formation, it is appropriate to consider only Schwarzschild BHs—which are adopted in this work.

The spatial grid is divided such that the resolution is concentrated in the accretion flow domain. Thus, the θ-grid is not uniform and chosen as

$$N_\mathrm{cell} \text{ in the } \theta\text{-direction} = \begin{cases} 10, & \text{if } \theta < 15^\circ \text{ or } \theta > 165^\circ \\ 380, & \text{if } 15^\circ < \theta < 165^\circ \end{cases} \tag{2.24}$$

which gives more focus on the equatorial plane than at the poles, where N_cell is the number of cells in the θ-direction.

The grid resolution is 400×400. The reason why the resolution in θ is slightly higher here compared to some of the other works in the literature is the following. When the radiative cooling turns on and if the density is large enough, the flow will collapse into a dense and cold thin disk. Therefore, more resolution in the equatorial plane is needed to properly model the dynamics of this region. The whole grid can be seen in Figure 2.3. A zoomed-in version showing the inner parts of the grid is displayed in Figure 2.4.

2.4.2 Initial torus

The initial condition for the torus is a stationary torus in dynamical equilibrium proposed by Papaloizou and Pringle (1984). In this work, the torus is in equilibrium under the three basic forces given in Eq. 2.25: gravitational ($\boldsymbol{F}_g$), rotational ($\boldsymbol{F}_r$) and forces due to the pressure of the fluid ($\boldsymbol{F}_P$).

Assuming axial symmetry and the equation of state $P = \kappa\rho^\gamma$ (where P is the pressure, ρ the density and γ the adiabatic index), it is possible to simplify the problem using the

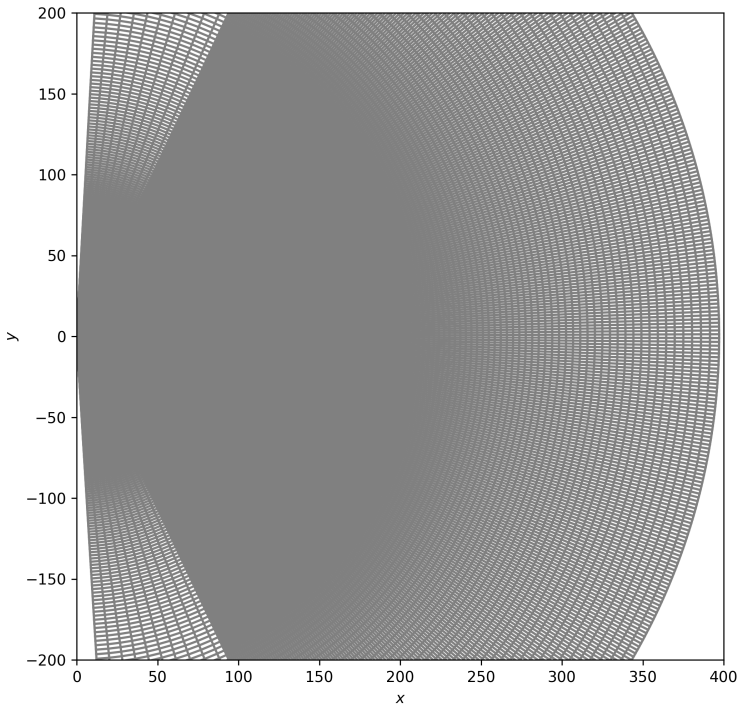

Figure 2.3: Grid used in all simulations of this work

potential formalism $\boldsymbol{F}_i = -\boldsymbol{\nabla}\phi_i$, which leads to Eq. 2.26, where C is an arbitrary constant, coming from the integration.

$$\boldsymbol{F}_g + \boldsymbol{F}_r + \boldsymbol{F}_P = 0, \tag{2.25}$$

$$\boldsymbol{\nabla}(\phi_g + \phi_r + \phi_P) = 0 \rightarrow (\phi_g + \phi_r + \phi_P) = C. \tag{2.26}$$

The pressure potential is given by the Eq. (2.27),

$$\boldsymbol{\nabla}\phi_P = \frac{\boldsymbol{\nabla}P}{\rho} \rightarrow \phi_P = \frac{\gamma}{\gamma - 1}\left(\frac{P}{\rho}\right) + \phi_{P,0}. \tag{2.27}$$

In the case of Papaloizou and Pringle (1984), a newtonian gravitational potential is used. However, for the purpose of this work, the equations are derived for the Paczynsky and Wiita (1980) potential (cf. Eq. 2.4).

For the rotational potential ϕ_r, it was assumed that the specific angular momentum is given by a power law. It is related to the angular velocity Ω by $l(r) = \Omega(r)r^2$ [2]. Thus, the

[2] Note that in this section r is the cylindrical radius and R is the spherical one.

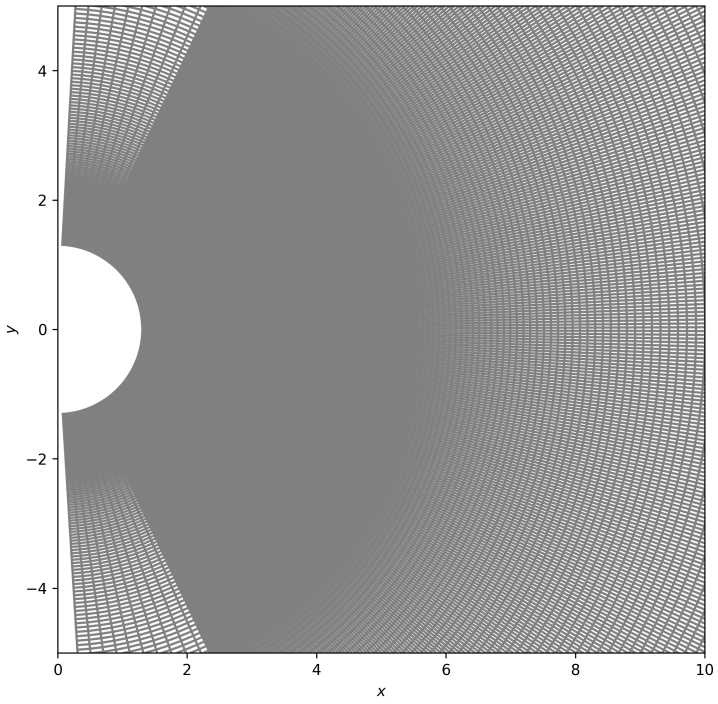

Figure 2.4: Zoomed-in version of Figure 2.3

angular momentum can be parameterized by

$$l(r) = l_0 \left(\frac{r}{r_0}\right)^a, \tag{2.28}$$

where r_0 is an arbitrary radius in which $l(r_0) = l_0$. For the purpose of this work, $a = 0$ will be used just as in Papaloizou and Pringle (1984), i.e. a constant specific angular momentum is assumed. Thus the "rotational potential" is given by

$$\phi_r = -\int dr \frac{l(r)^2}{r^3} = \frac{l^2}{2r^2} + \phi_{r,0}. \tag{2.29}$$

As a pseudo-newtonian gravitational potential is being used, it is necessary to use the keplerian specific angular momentum, given by

$$-\boldsymbol{\nabla}\phi_g(r) + \hat{r}\frac{l_K^2}{r^3} = 0 \Rightarrow l_K^2(r) = r^3 \frac{d\phi_g(r)}{dr} = \frac{GMr^3}{(r - r_S)^2} \tag{2.30}$$

Now, to solve the Eq. 2.26, it is necessary to make some assumptions. First, axisymmetry is adopted. Second, it is important to set up some essential constants: $r_{\min}$ is the

inner radius of the initial torus, r_0 is the radius where the density is at its maximum (by symmetry, it should be in the $z = 0$ plane) and ρ_0 is the value of the density in $(r_0, z = 0)$. The resulting density is

$$\rho = \left[\frac{\gamma - 1}{\kappa\gamma}\left(C - \phi_g(R) - \phi_r(r)\right)\right]^{\frac{1}{\gamma-1}}, \tag{2.31}$$

where C and κ are defined from the boundary condition, written as

$$C = \phi_g(r_{min}) + \phi_r(r_{min}), \tag{2.32}$$

$$\kappa = \frac{\gamma - 1}{\gamma}\left[C - \phi_g(r_0) - \phi_r(r_0)\right]\rho_0^{1-\gamma}. \tag{2.33}$$

The definition given for r_0 from Eq. 2.28 forces l_0 to be the keplerian specific angular momentum (Eq. 2.30) in $r = r_0$, since there is no force due to pressure at this place ($\boldsymbol{\nabla} P = 0$). It is obtained that

$$l_0^2 = l_K^2(r_0) = \frac{GMr_0^3}{(r_0 - r_S)^2} \tag{2.34}$$

Finally, the important parameters that describe the shape of the torus are $r_{\min}$, r_0 and ρ_0. For this work, the size of the initial torus was chosen by setting $r_{\min} = 75R_s$ and $r_0 = 100R_s$, which gives a torus extending all the way to $r_{\max} = 150R_s$ as can be seen in Figure 2.5.

The ρ_0 parameter is set according to the accretion rate wanted for the simulation, because it is basically controlled by the total amount of mass available for the BH to accrete. One thing to note is that if the simulations were adiabatic (i.e. no radiative cooling included), the results would be scale free meaning that it would be possible to scale the results to any values of ρ_0 and M after the simulation was finished. However, since radiative cooling was taken into account in these simulations, both the parameters ρ_0 and M turn out to be essential to determine the overall importance of cooling—as cooling gets more important with increasing accretion rate (Wu et al., 2016; Narayan et al., 1998)—and the relative importance of the cooling mechanisms because they depend with different powers on the mass.

Another important point is that the density outside of the initial torus, referred to here as the "atmosphere", is not set to zero (i.e. a vacuum) as it should be for technical reasons. Instead, it is assumed to be $\rho_{\text{amb}} = 10^{-4}\rho_0$, which is small enough to not affect the general results and is not so small that it would cause numerical problems due to numerical fluctuations that could lead to non-physical results as negative density.

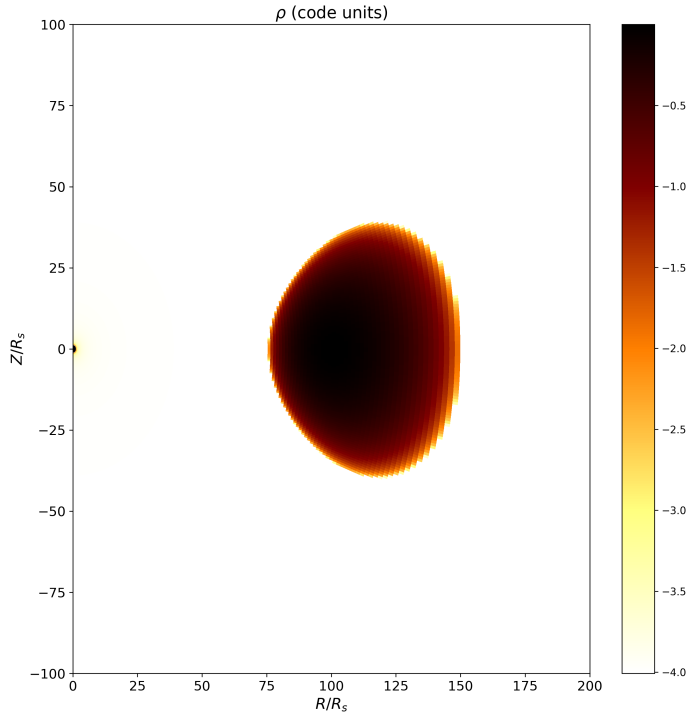

Figure 2.5: Torus initial condition in hydrodynamical equilibrium following Papaloizou and Pringle (1984). Here, $r_{\rm min} = 75R_{\rm s}$ and $r_0 = 100R_{\rm s}$, which gives a initial torus extending all the way up to $r_{\rm max} = 150R_{\rm s}$.

2.4.3 β parameter

For HD simulations there are no magnetic fields; however, the presence of magnetic fields is essential for synchrotron and comptonized synchrotron emission. Thus, it is necessary to use some approach to estimate the expected field strength which will be used to calculate the cooling processes.

What is usually done in these cases is to assume the presence of a local, isotropic, randomly tangled magnetic field in the flow and quantify its importance using the plasma-β parameter given by $\beta = P_{\rm gas}/P_{\rm mag}$. Equipartition between gas pressure and magnetic pressure is assumed such that $P_{\rm gas} = \rho c_s^2$ with $P_{\rm mag} = B^2/8\pi$. Therefore, it is possible to obtain an approximation for the magnetic field strength, given by

$$B^2 = \frac{8\pi\rho c_s^2}{\beta}. \tag{2.35}$$

Wu et al. (2016) has a whole discussion of the effects of different values of β. Their fiducial model adopts $\beta = 10$, which is also the values adopted in the present work. This value is appropriate for this approximation because it is known that this kind of system is

dominated by gas pressure, so $\beta > 1$. If $\beta \gg 1$, the effect would be negligible (see Yuan and Narayan, 2014, for a more detailed review).

2.4.4 Temperature approximation

RIAFs should be characterized by a two-temperature plasma (Narayan and Yi, 1995; Yuan and Narayan, 2014). In this context, this means that the electron temperature in the inner region of the accretion flow is considerably lower than the ion temperature. This happens because electrons can cool more efficiently than ions due to the large mass difference between the particles, and also their adiabatic index are different which means that at high temperatures ($T \gtrsim 10^{10}$K) electrons become relativistic while ions do not. Figure 2.6 shows approximately the temperature difference between the species in a RIAF.

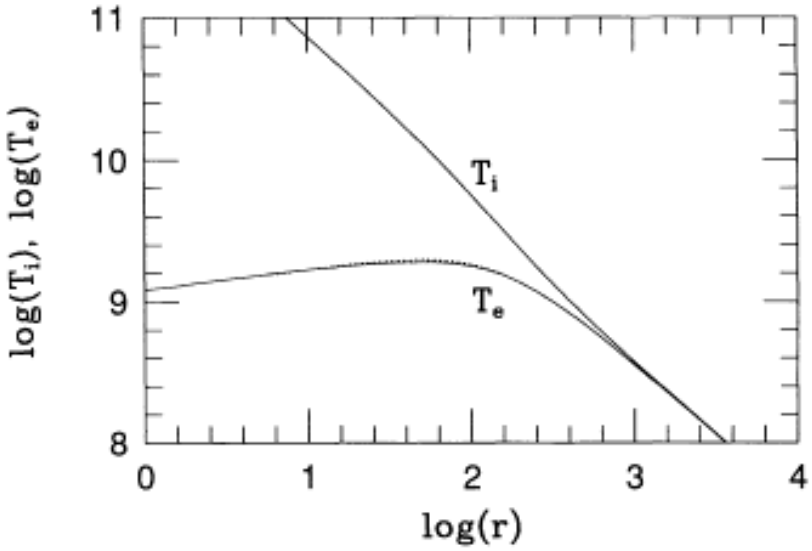

Figure 2.6: Temperatures of ions and electrons in a a RIAF as a function of the distance from the BH. Figure taken from Narayan and Yi (1995).

The following formula incorporates the results from the height-integrated treatment of accretion flows on the temperature difference between electrons and ions:

$$T_{\mathrm{e}} = \frac{T_{\mathrm{ion}}}{(R/r_0)^{-1} + 2.0}, \tag{2.36}$$

where r_0 is the radius where the density is at its maximum (Wu et al., 2016) and where T_{ion} is taken from the simulation, being

$$T_{\mathrm{ion}} = \frac{p}{\rho}\frac{\mu m_{\mathrm{u}}}{k_{\mathrm{B}}}. \tag{2.37}$$

The effect of Eq. 2.36 can be seen in Figure 2.7 which shows the behavior of the electron and ion temperature as a function of the radius.

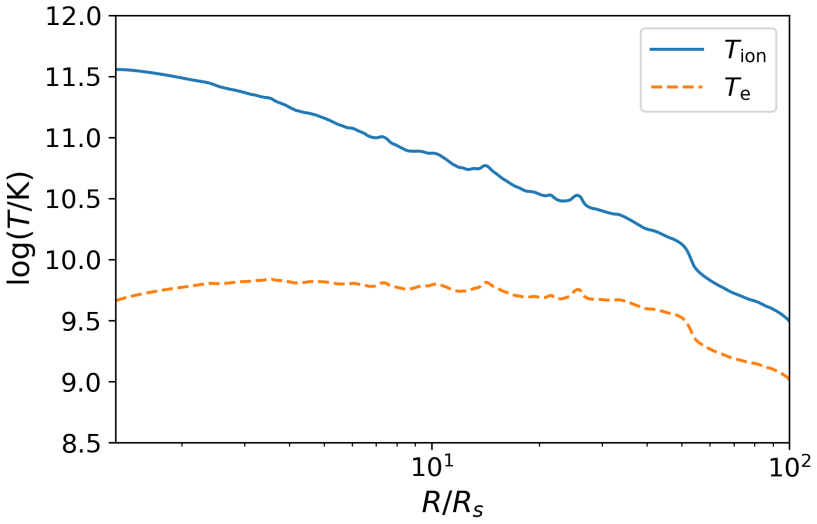

Figure 2.7: Radial dependence of the ion and electron temperatures from eq. 2.36. The data used to compute the temperatures come from the simulation snapshot displayed in Figure 2.8. Note that the temperatures are compatible with the results from Figure 2.6, although the electron temperature is ~ 3 times higher than the predicted in Narayan and Yi (1995).

2.4.5 *Radiative cooling*

The approach adopted here to incorporate the radiative cooling is the following. Before the radiative cooling is "turned on", the simulation is first evolved without any cooling until the flow reaches a quasi-steady state. This state is characterized by an almost constant accretion rate over timescales of $5000GM/c^3$. The quasi-steady state is a proxy to judge when it is safe to switch on the radiative cooling—to judge when the accretion flow has achieved inflow equilibrium (Narayan et al., 2012). The value of $\dot{M}$ from the simulations is never constant because of the effect of convective turbulence (and MRI turbulence if magnetic fields were present).

Figure 2.8 shows the exact simulation snapshot at which cooling is turned on, when it is judged that quasi-steady state has been reached. Figure 2.9 shows the $\dot{M}$ time series, where it is indicated the time at which cooling is turned on. This precaution is done to avoid numerical errors and to avoid non-physical effects.

The beginning of all simulations without radiative cooling is the same: radiative cooling

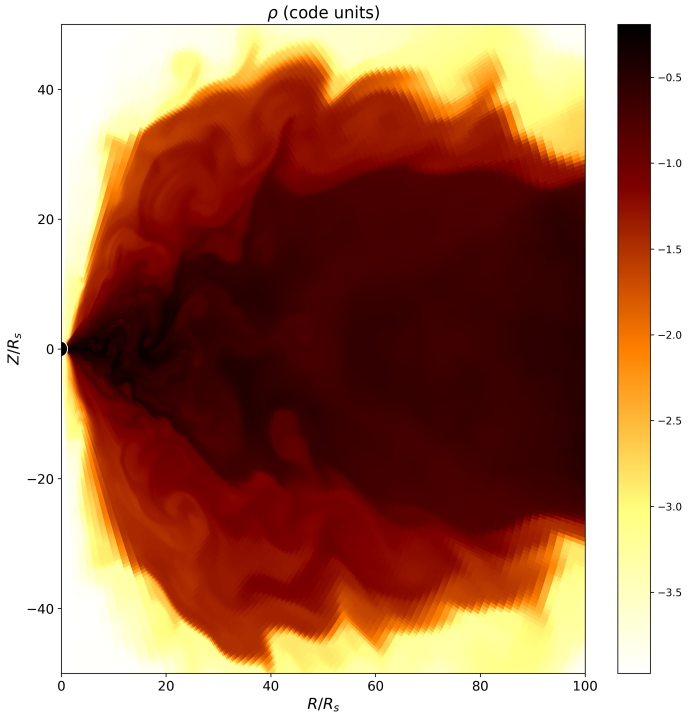

Figure 2.8: Accretion flow state when it reaches the quasi-steady state. At this point in the simulation, radiative cooling is turned on.

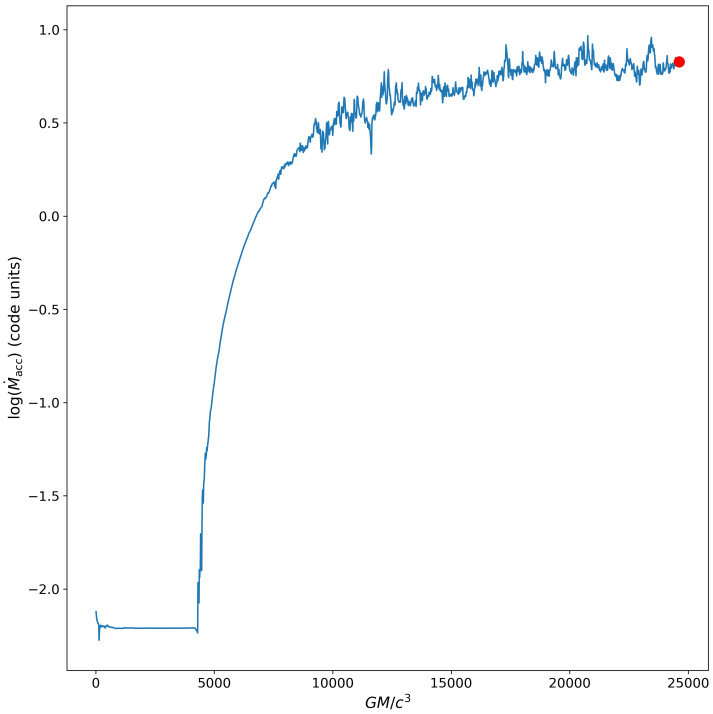

Figure 2.9: Accretion rate of an arbitrary simulation indicating when the radiative cooling is turned on. The moment when cooling is activated is indicated by a red dot.

is turned on at $t = 1.4t_{\rm orb}$, where

$$t_{\rm orb} = \frac{2\pi r_0}{v_{\phi 0}} \simeq 17506 \frac{GM}{c^3}. \tag{2.38}$$

is the orbital time of the accretion flow in $R = r_0$.

Chapter 3

Analysis and results

In section 3.1 the general properties of the accretion flow are described, comparing them with the properties expected from analytical models. In section 3.2, the relation between the truncation radius and the mass accretion rate is presented, comparing it with observations. Finally, in section 3.3, the properties of the hot corona will be presented.

3.1 Accretion flow properties

In this section all the five simulations carried out in the work will be described. Table 3.1 displays the main parameters that describe each model, together with the results for the truncation radius of the simulations.

Table 3.1 - Main parameters of the simulations and the resulting truncation radii.

ID	$\dot{M}_{\rm acc}/\dot{M}_{\rm Edd}$	$R_{\rm tr}/R_{\rm s}$
1	0.35 ± 0.09	11.2 ± 2.5
2	0.24 ± 0.07	13.2 ± 2.7
3	0.11 ± 0.02	20.3 ± 5.3
4	0.06 ± 0.01	27.5 ± 5.8
5	0.02	-

A snapshot from each simulation can be seen in Figures 3.1 and 3.2, where the density and the temperature maps are shown respectively. They were taken at $t = 2t_{\rm orb} =$

$34112GM/c^3$. The first thing to notice here is the formation of a very dense (10-100 times denser than the torus before the radiative cooling; cf. Figure 2.8) and thin accretion disk at the equatorial plane. The second is that this thin disk is embedded in a very hot corona ($T \sim 10^{10-11}K$) and is very cold compared to the surrounding corona. This behavior is expected as explained in the section 1.2, where there is a coexistence of both cold and hot phases (thin disk + RIAF) and is consistent with other simulations with radiative cooling (Wu et al., 2016; Das and Sharma, 2013).

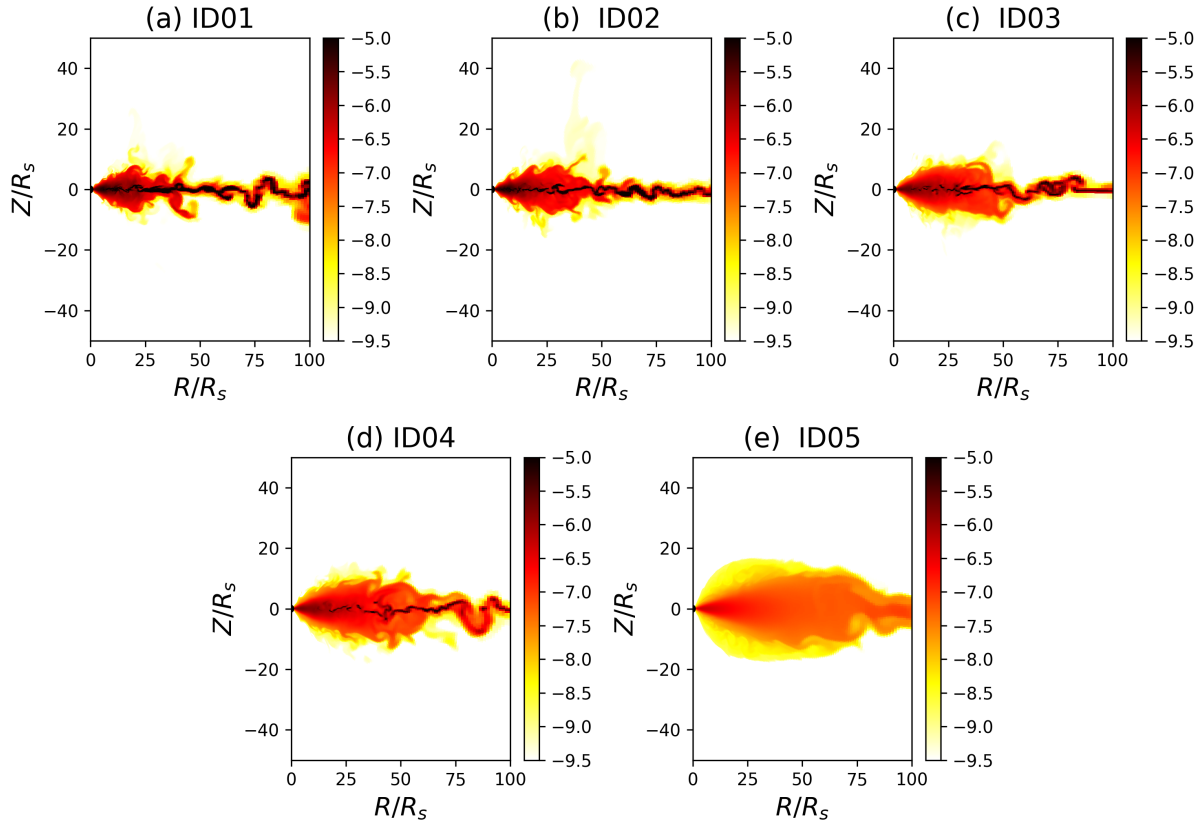

Figure 3.1: Density maps of the five simulations carried out in this work. The colors indicate the log of the density in g cm^{-3}. They were taken at $t = 34112GM/c^3$, which corresponds to $2t_{\rm orb}$, a value between the ranges used in Figure 3.3. For each model, a different mean accretion rate is set by hand, changing the unit density in the code. The accretion rates are listed in Table 3.1.

Besides that, it is possible to note in Figures 3.1e and 3.2e that when the accretion rate is lower than a certain critical value ($\dot{m}_{\rm acc} \lesssim \dot{m}_{\rm crit}$, where $\dot{m} = \dot{M}/\dot{M}_{\rm Edd}$) the accretion flow does not collapse into a thin, dense and cold disk, instead it remains very hot, low-density and geometrically thick. This is expected because as the accretion rate gets lower the density gets lower, and the gas starts becoming inefficient in radiating i.e. the cooling time

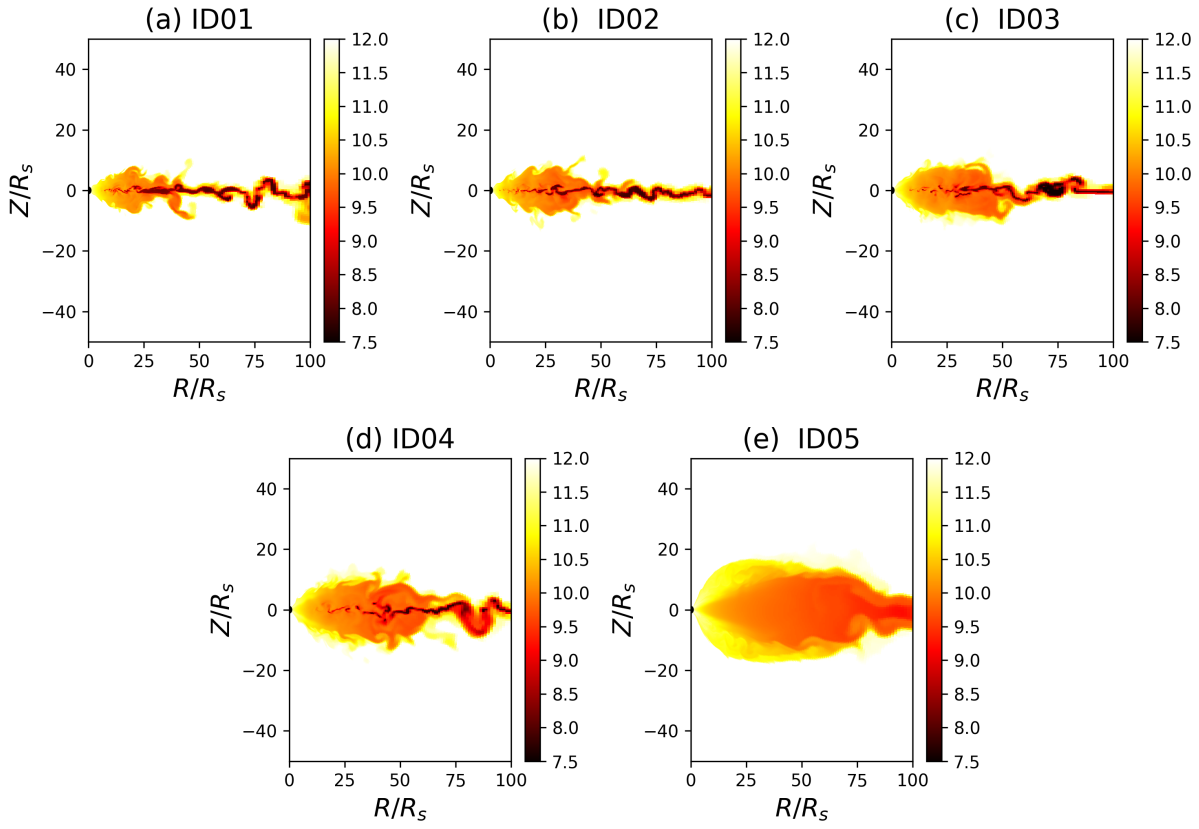

Figure 3.2: Temperature maps of the simulations for $t = 34112GM/c^3$. The colors indicate the log of the temperature in units of K.

is longer than the viscous time.

In this work, a value of

$$0.06 > \dot{m}_{\rm crit} \gtrsim 0.02 \tag{3.1}$$

is found. This can be written in terms of the α-parameter, $6\alpha > \dot{m}_{\rm crit} \gtrsim 2\alpha$. This is the first result of this work and is consistent with the results of Wu et al. (2016), where $\dot{m}_{\rm crit} \sim 3\alpha$. However, it is not consistent with the value given by Narayan and Yi (1995) and Xie and Yuan (2012), where $\dot{m}_{\rm crit} \sim \alpha_{\rm SS}^2$, although they adopt the α-viscosity of Shakura and Sunyaev (1973), which is slightly different from the one defined by Stone et al. (1999) which is adopted in this work.

As a clarification, the mass accretion rate is calculated using

$$\dot{M}_{\rm acc} = 2\pi r^2 \int_0^\pi \rho v_{\rm r} \sin\theta \, d\theta. \tag{3.2}$$

This is based on the traditional approach pioneered by Stone et al. (1999) (cf. their equation 8). This is the flux of material through a sphere with radius R. The value of

$\dot{M}_{\rm acc}$ in Table 3.1 was computed at the inner boundary of the simulations, where $R = 1.3R_{\rm s}$.

In the simulations, there is no mass injection. As the models are evolved, the mass in the computational box decreases which can lead to issues and can affect the long-term evolution of $\dot{M}$. For this reason, the mean value of $\dot{M}_{\rm acc}$ is computed over a certain range of time during which it remains relatively constant. The temporal ranges used for computing $\dot{M}_{\rm acc}$ are shown in Figure 3.3.

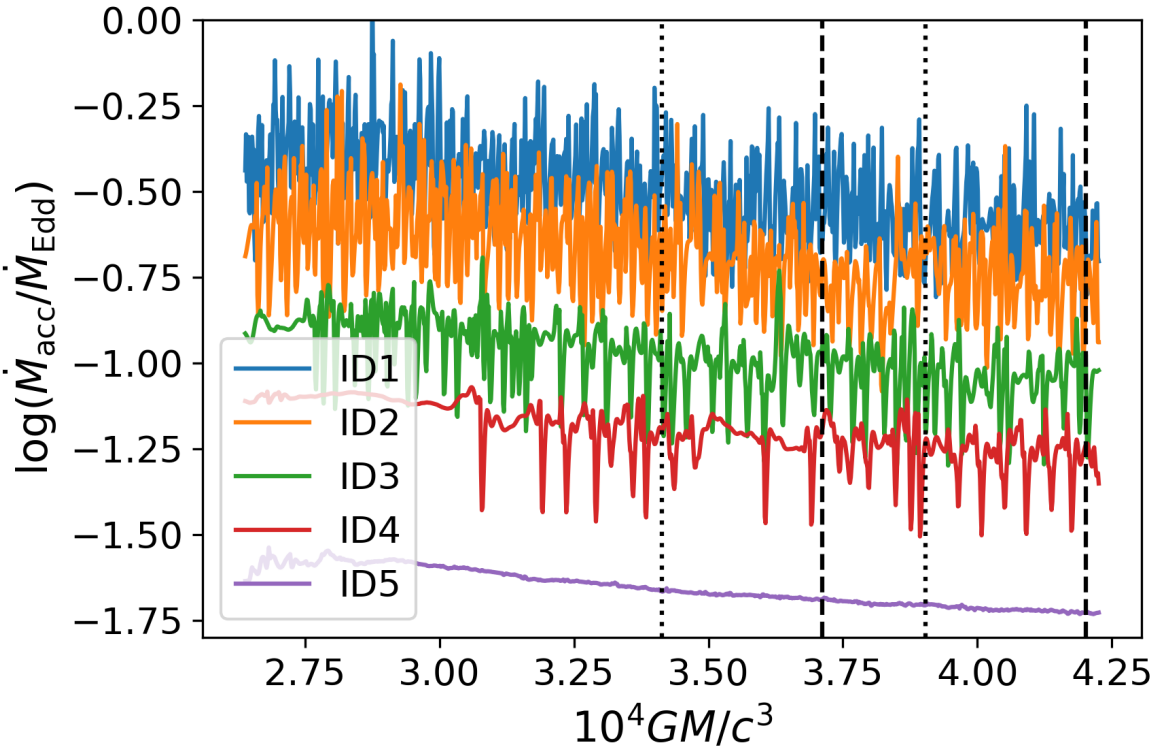

Figure 3.3: Temporal evolution of the mass accretion rate of all simulations after the radiative cooling is turned on. Here, the accretion rate is shown until $t = 2.5t_{\rm orb} = 42640GM/c^3$, which is the range of time that is interesting for the work. The dotted black lines span a range of time from $32400GM/c^3 - 37520GM/c^3$ used for the simulation ID4 and ID5 and the dashed line from $35815GM/c^3 - 40930GM/c^3$ used for the other simulations. These ranges were chosen where the accretion rate is almost constant.

3.1.1 Dependency of the variables

In this subsection the dependencies of the variables $\rho, v_{\rm r}, v_\phi$ and T on the distance from the BH will be presented. All the variables are time averaged between $1.6t_{\rm orb}$ and $1.8t_{\rm orb}$ and are taken from the equatorial plane to be more representative of the thin disk.

As is possible to see in the top left image from Figure 3.4, the density in the simulation with radiative cooling can get 100 times denser than the simulation where $\dot{m}_{\rm acc} < \dot{m}_{\rm crit}$ (ID5).

A radial power-law function was fitted to the four variables displayed in Figure 3.4 in order to characterize the corresponding slopes. For example, in the case of the density, the function $\rho(r) = Ar^p$ was fitted to the numerical data from the simulation where A is a constant, resulting in $p = -1.25$; this value is similar to the prediction for a RIAF with mass-loss, $p < -1.5$ (the ADIOS model of Blandford and Begelman 1999; Yuan and Narayan 2014). On the other hand, for the thin disk the power-law dependency is -1.45, whereas the value predicted for a Shakura and Sunyaev (1973) accretion disk is -1.88 (Frank et al., 2002). Note that for the RIAF, ID5 simulation was used, because there is no formation of cold clumps or thin disk, and for the thin disk, ID1 was used, because it is the simulation with the smallest truncation radius.

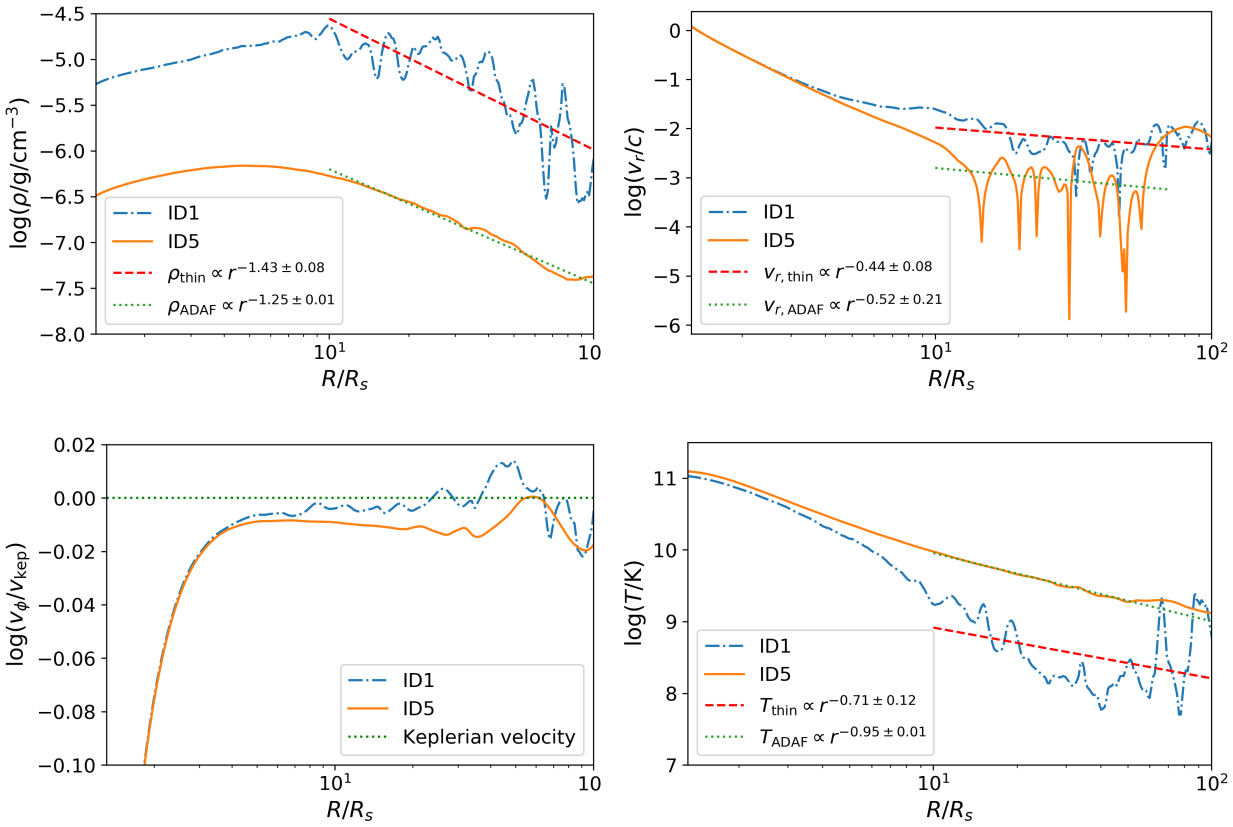

Figure 3.4: Comparison of the radial dependency of the density, radial velocity, orbital velocity and temperature for both hot and thin phases. Top left: density; top right: radial velocity in terms of the speed of light; bottom left: angular velocity in keplerian units; bottom right: temperature.

Similarly to the density, a power-law was fitted to the radial velocity in the top right

image. v_r of the RIAF has a slope of -0.52, which is consistent with the -0.5 value predicted from the self-similar solutions of Yuan et al. (2012), although the uncertainty is very high. For the thin disk, the radial velocity predicted here is much higher than the expectation for a Shakura and Sunyaev (1973) disk. This is because the accretion theory predicts that $v \sim \alpha c_s H/R$, and the aspect ratio and the sound speed for a thin disk is low, and is lower than a RIAF, which means that the radial velocity of a thin disk should be at least smaller than the hot accretion flow. This big difference is essentially because of the treatment given to the processes of cooling, which will be discussed later at the end of this subsection. The slope is also not consistent with the predicted -0.25 values (Frank et al., 2002; Shakura and Sunyaev, 1973).

It should be noted that the slopes predicted from the analytical calculations are a useful guide to the numerical models. However, the analytical and numerical models will not necessarily give the same results because our simulations include the time and more physics than the more simple calculations of Narayan and Yi (1995) and Shakura and Sunyaev (1973)—otherwise there would be no point in carrying out the simulations.

The angular velocity is the only variable in which the dependency is compatible with the theory. For the Shakura and Sunyaev (1973) disk, the angular velocity is keplerian (Frank et al., 2002), as it is shown in the bottom left image of the Figure 3.4. For the RIAF, the simulation predicts it is sub-keplerian, in agreement with the theory (Yuan and Narayan, 2014), although it is only slightly sub-keplerian.

At last, the power-law slope of the temperature for both RIAF and thin disk are consistent with the theory. The RIAF temperature is virial (i.e. $\propto r^{-1}$) and the thin disk has a slope of -0.71, consistent with the $-3/4$ (Frank et al., 2002). The thin disk in the simulations is hotter ($T \sim 10^{7.5}$K) than a Shakura and Sunyaev (1973) disk ($T \sim 10^{4-6}$K). This feature may not be a problem, because in the simulations there are more physics included than the analytical calculations, as mentioned before.

The differences between the structure of the simulated thin disk and that predicted by Shakura and Sunyaev (1973) are due to several reasons. First, the Shakura and Sunyaev (1973) disk adopts Kramer's law opacity, which is not taken into account here. Secondly, the techniques used for the radiative cooling (specially for the optically thick disk) has a lot of approximations and does not take into account radiative transfer, which is important for the comptonization process. It is expected that, improving these treatments and im-

plementing magnetic fields in the simulations, the structure of the thin disk will eventually become more similar to a Shakura and Sunyaev (1973) disk.

3.2 Truncation radius

This section describes the main result of this paper: the relation between the truncation radius, or the transition radius between the outer thin disk and the RIAF, and the mass accretion rate.

The first thing to describe is how the truncation radius was estimated from the simulations. Our simulations do not tell us directly where the cold thin disk is. This is similar to the situation in many numerical astrophysical simulations where there is a physical property of interest but the simulation does not give the number directly; instead, a search mechanism for the property of interest must be explicitly designed—e.g. in n-body cosmological simulations of structure formation, the meaning of a dark matter halo must be defined before they can be identified (Vogelsberger et al., 2014). Here, firstly a concrete definition of a thin disk is given, then the thin disk is identified and the transition radius estimated from the simulated arrays.

The focus is on identifying the colder, denser equatorial region of the accretion flow and characterizing its thickness and the point at which it transitions to a hotter phase. Concretely, whenever a thin disk is formed, its density is at least ten times larger than the surrounding RIAF. In addition, the thin disk's temperature is at least ten times lower than the RIAF's. For practical purposes, the cold thin disk phase is defined to occur whenever the colder, denser gas has $H/R < 0.015$, which is consistent with the expectations from the theory of thin disks according to which H/R should be in the range $10^{-3}-0.01$ (Piran et al., 2015; Frank et al., 2002). The thin disks in our simulations settle to vertical equilibrium with $H/R > 4 \times 10^{-3}$. Our results are not very sensitive to the particular value of the threshold thickness as long as it is not much larger than 0.01.

The method for estimating the transition radius is now described. First, the density array was converted from the native polar coordinates adopted in `PLUTO` to cylindrical coordinates—a procedure called regridding for which GPU-accelerated routines written by the group are used for faster calculations. The density values at each cylindrical radius are obtained in the $R-z$ plane (Figure 3.5).

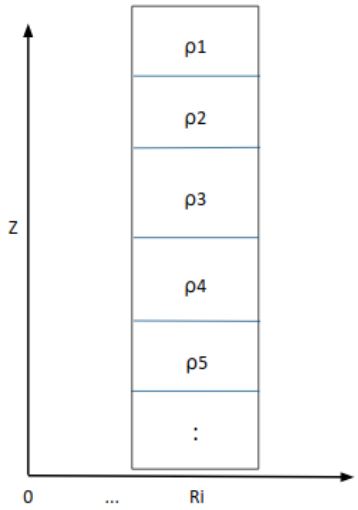

Figure 3.5: Schematic example illustrating how the scale height H/R was obtained from the simulation. For each R_i (R_i here refers to the cylindrical radius), the corresponding one-dimensional array with the density was selected and a Gaussian was fitted. The width σ of the Gaussian gives approximately H.

At each value of R, the vertical density distribution of the accretion flow resembles the superposition of two Gaussian functions centered at $z = 0$ (the midplane of the disk): one Gaussian with a low amplitude and small width corresponding to the thin disk phase whenever it occurs, and a second, large amplitude, broader Gaussian that describes the RIAF phase. The $\rho(R, z)$ distribution for several snapshots of the simulations were carefully inspected in order to verify the above statements.

At each value of R, a Gaussian function was fitted in order to characterize the vertical density distribution. One example is displayed in Figure 3.6. Whenever the disk collapses into a thin disk, the density increases by a factor of $10 - 100$ times the RIAF equatorial density. The width σ of the Gaussian fit will in this case probe the vertical density distribution of the thin disk instead of the RIAF, as argued in the previous paragraph.

In summary, with the method outlined above it is possible to estimate the aspect ratio H/R of the thin disk as a function of R for each time step of the simulation, as illustrated in Figure 3.7. The same time range used for the calculation of the mass accretion rates (cf. Figure 3.3) is also used to compute the truncation radius. More specifically, the value of R at which the mean value of the based on 80 points (from smaller to larger R) at which $H/R < 0.015$ is taken to be the inner radius of the thin disk.

As it can be seen in Figure 3.7, the transition between a hot accretion flow ($H/R \sim 0.1$)

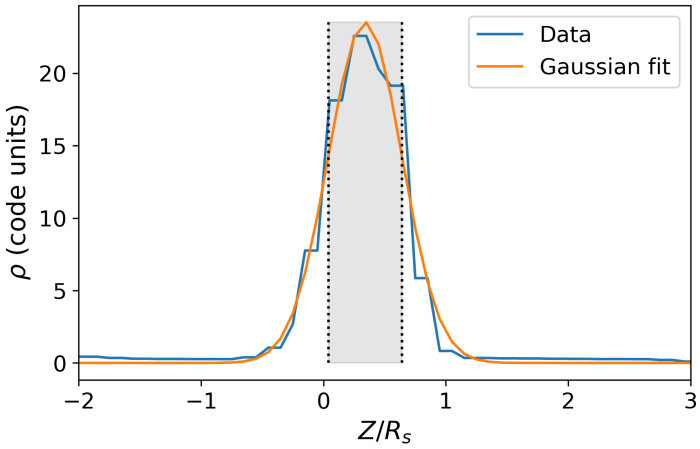

Figure 3.6: Example of a Gaussian fit to the vertical density distribution of the accretion flow to estimate the thickness of the disk. Here, the shaded area indicates the 1σ width of the Gaussian. The accretion flow in this particular snapshot contains a thin disk.

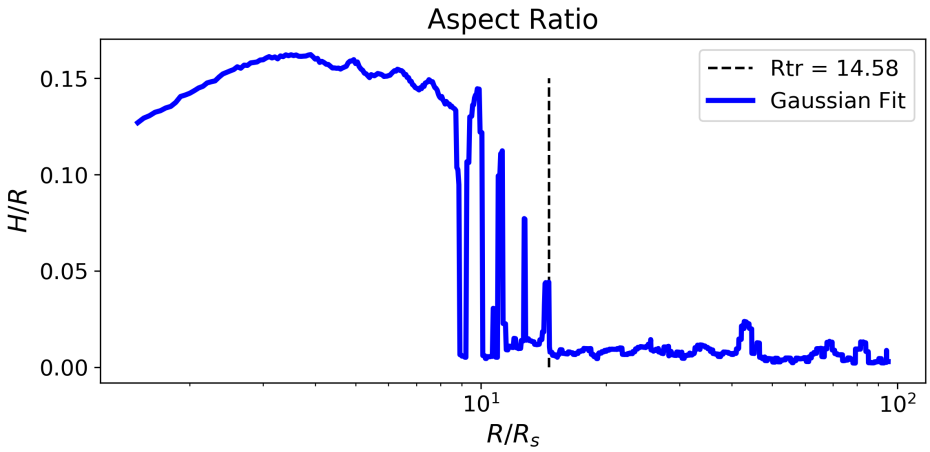

Figure 3.7: Disk thickness H/R as a function of the cylindrical radius R/R_s (i.e. the distance from the BH). The dashed line indicates the truncation radius, i.e. the point at which H/R becomes smaller than 0.015.

and the cold thin disk ($H/R \lesssim 0.01$) is not precise which makes it hard to define exactly where the truncation radius begins. The definition used in this work ensures that the truncation radius is located where the oscillations in the value of H/R reaches a minimum (cf. dashed line in Figure 3.7). Although the location of the truncation radius is not exact, this rough estimate obtained with this approach should be enough for our purposes of quantifying the relation between the truncation radius and the accretion rate.

The final truncation radius for each model corresponds to the median value of the

truncation radii obtained from each time step and the uncertainty is given by the standard deviation. Each time step corresponds to a point in Figure 3.8. Figure 3.8 displays the results for the 4 simulations where thin accretion disk were formed.

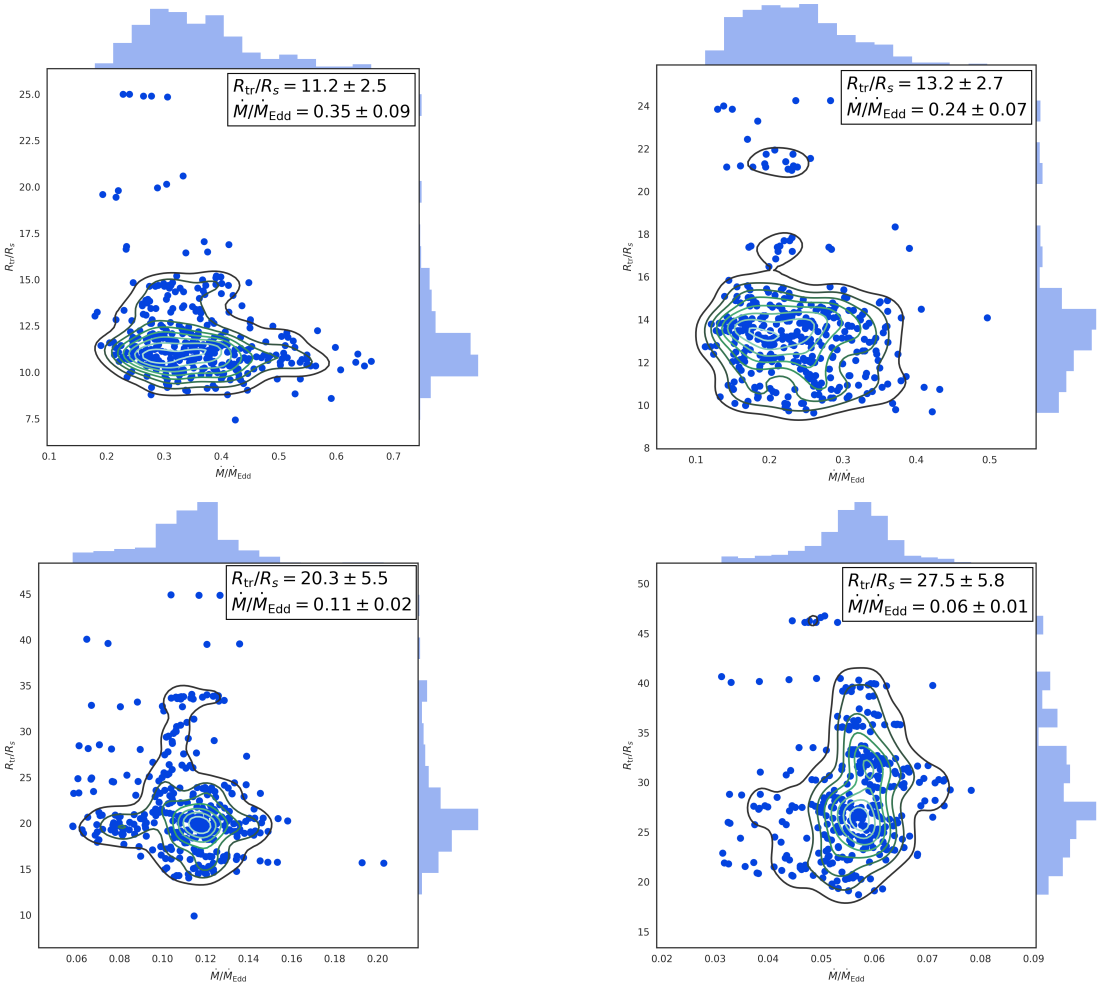

Figure 3.8: Distribution of truncation radii (or inner radius of the thin disk) in units of the Schwarzschild radius for each model, as a function of the mass accretion rate in Eddington units. Each image corresponds to one of the simulation: top left is ID1; top right is ID2; bottom left is ID3; and bottom right is ID4. Each point corresponds to a different timestep used to estimate $r_{\rm tr}$ from a model. The distributions on top and to the right of each panel correspond to the histograms of each variable.

With these results it is now possible to assess the relation between the thin disk truncation radius and the mass accretion rate, displayed in Figure 3.9. A power-law fit to the numerical data results in $R_{\rm tr} \propto \dot{m}^{-1/2}$.

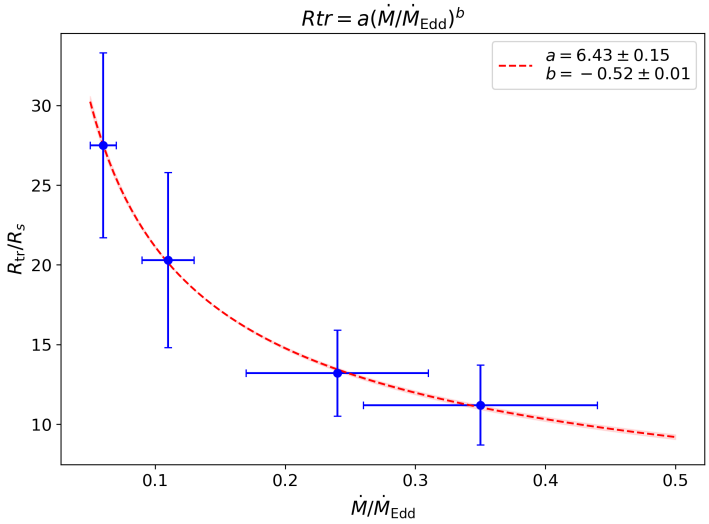

Figure 3.9: The relation between the truncation radius and the mass accretion rate. The blue circles indicate the points from this work. The red dashed line shows the power-law fit obtained in this work: $R_{\rm tr}/R_{\rm s} = 6.4\dot{m}^{0.52}$.

3.3 Contraction and cooling of hot corona

In this section, the hot corona will be studied. More precisely, its extension and temperature will be characterized. By extension here it is meant both its vertical thickness and lateral extension.

The vertical thickness is given by the corona scale height. This is computed following the procedure adopted for calculating the thickness of the thin disk described in section 3.2. There is one difference though: as the thin disk is denser than the corona, the Gaussian contributed by the thin disk will dominate in the estimates. Therefore, the denser part corresponding to the thin disk needs to be removed for the calculations involving the corona.

To accomplish that, the following simple procedure is adopted: a density threshold is set; if the density at any point is higher than this threshold, the gas at that region is substituted by the value of the threshold. This is represented in Figure 3.10, where it is possible to see what happens with the accretion flow after applying the threshold—the corona now dominates. The threshold chosen here was $\log(\rho/\rho_0) \geq -0.5$. This value eliminates the region of the disk that is $10 - 100$ times denser than the corona, and keeps the lower density gas of the corona.

Before applying of threshold density cut, the snapshot of each time step in the same

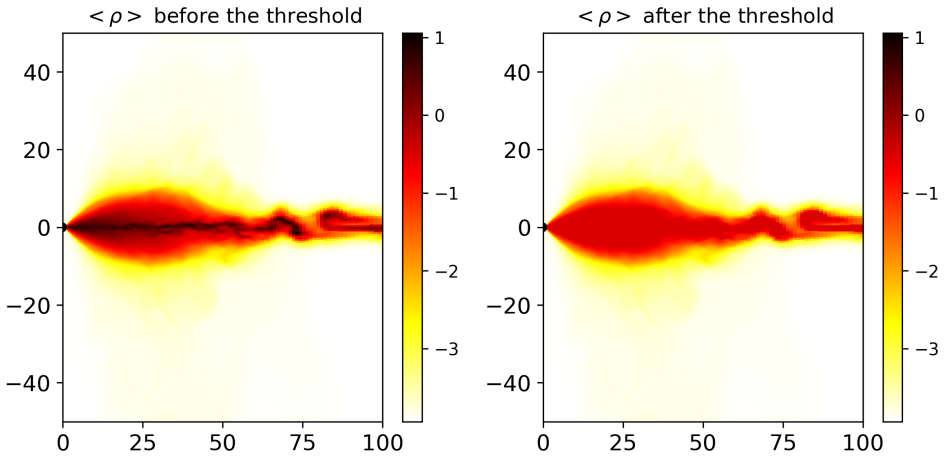

Figure 3.10: Application of the procedure to remove the thin disk contribution. Here, the time-averaged density of model ID3 is displayed. Following this procedure, it is possible to estimate the scale height, i.e. the vertical thickness of the corona.

range of values used to calculate the truncation radius (and shown in Figure 3.3) is taken and an average of the density values in time is done. Then, the threshold is applied. After that, a Gaussian is fitted and then, as the corona has a big gradient in density, the height of the corona is assumed to be equal to $2H$, where $H \sim \sigma$ (σ is the Gaussian width).

For the lateral extension of the corona, it is assumed to have an elliptical-like shape. Figures 3.1 and 3.10 demonstrate that this is indeed a very good approximation. Its lateral extension is twice the location where the maximum height happens, which means that if the vertical height of the accretion flow is at $z = 10R_{\rm s}$, its extension would be $20R_{\rm s}$.

Figure 3.11 shows that the corona tends to contract as the accretion rate increases—both its height and lateral size. This is one of the two main results from this work, together with the correlation between the thin disk inner radius and $\dot{m}$.

Another feature which is worth being estimated from the simulations is the coronal temperature. To analyse only the corona, eliminating everything that is not the hot corona is necessary. In order to achieve that, both a tracer (cf. Section 2.2.3) and a temperature threshold are adopted in order to eliminate the contribution of the cold disk (instead of simply using a density threshold). The threshold corresponds to discarding all regions of the flow at which the temperature is lower than 10^9K. Figure 3.12 shows an example of density map after eliminating both the atmosphere and the thin disk are shown. Note that the temperature is time-averaged in the same range used before.

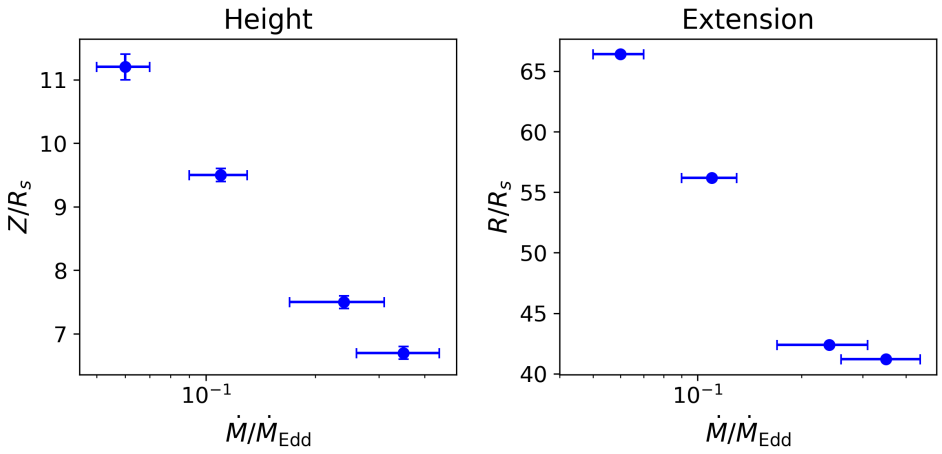

Figure 3.11: Height and extension of the corona as a function of the mass accretion rate. The corona contracts as $\dot{m}$ increases.

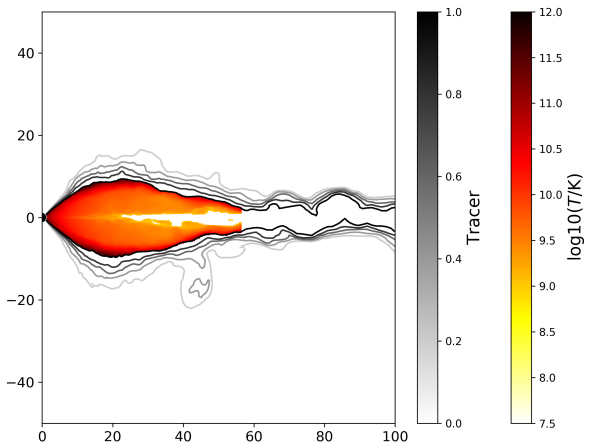

Figure 3.12: Example of what the coronal temperature map looks like after removing all features but the corona, for the purposes of characterizing the coronal temperature. This figure corresponds to model ID3. The lines denote a contour plot of the tracer. Note that the entire accretion flow is contained within the lines with values of ~ 1.

Following this procedure, the median value of the coronal temperature for every simulation which has a cold thin disk (i.e. models ID1-ID4) was computed. Figure 3.13 shows the resulting relation between the median coronal temperature and $\dot{m}$. This figure shows that the temperature of the corona tends to decrease with increasing mass accretion rate, if only slightly.

This can be explained by looking at the rate of collisional energy transfer from ions to

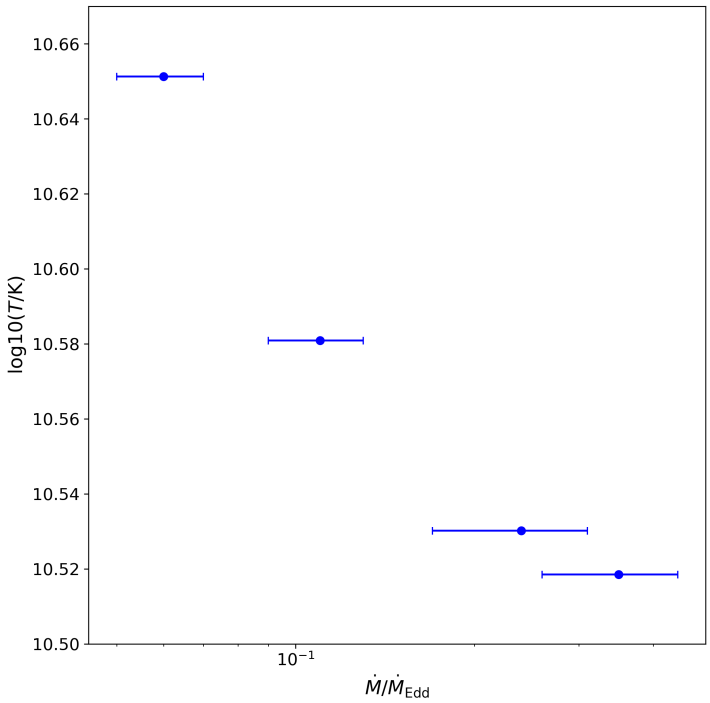

Figure 3.13: Median coronal temperature as a function of the mass accretion rate. It is possible to see that the corona cools very slightly, from 4.5×10^{10} K to 3.3×10^{10} K.

electrons equation, given by Stepney and Guilbert (1983) and approximated as

$$Q_{\rm col} = 1.639 \times 10^{-17} n_e n_i \frac{T_i - T_e}{T_e^{3/2}} \tag{3.3}$$

where T_i is the ion temperature, T_e is the electron temperature, n_i the ion number density and n_e the electron number density. This equation shows that when the electron temperature decreases the energy transfer increases, which means that the ion temperature decreases, because there will be more energy being transferred from ions to electrons. This will happen because as the accretion rate increases, the radiative cooling also increases, which in this case will make the electron temperature decrease, decreasing the ion temperature.

Chapter 4

Discussion

4.1 *Comparison with observations*

In this section, a comparison is made between the results of the model and observations of stellar-mass BHs.

The observational data used to compare with this work's results are from Garcia et al. (2015), regarding the source GX 339-4. This system is one of the most studied BHXRBs. Garcia et al. (2015) analysed and reduced the data from the Principal Counter Array (PCA) detector on board of the Rossi X-ray Timing Explorer (RXTE). The analysed data comes from 6 regions (from A to F) in the hard state of the system, as shown in the hardness-intensity diagram in Figure 4.1.

The truncation radius in Garcia et al. (2015) is estimated by modeling the reflection spectrum of the system, mainly the Fe K line in the 6-8 keV energy range. For that, they assumed a fixed value of the spin parameter of $a_* = 0.998$ and fitted the spectrum of the 6 regions using their canonical Model 3 (check Table 3 from Garcia et al., 2015), as can be seen in Figure 4.2. Besides that, the luminosity was estimated assuming a distance of 8 kpc and a mass of the BH of $10M_\odot$, and was based on the fluxes computed over the 1-100 keV band (check Table 1 from Garcia et al., 2015).

Figure 4.3 displays the observational results from Garcia et al. (2015). Note that Garcia et al. (2015) quotes the source luminosity L instead of $\dot{m}$, so it is necessary to convert it to $\dot{m}$ for an appropriate comparison. The conversion from L to $\dot{m}$ was carried out using the equation $L = \eta \dot{M} c^2$ with the efficiency of conversion of accreted rest-mass energy into radiation η given by

$$\eta(R_{\rm tr}) = \frac{R_{\rm g}}{2R_{\rm tr}} \left(1 - C\left(\frac{R_{\rm out}}{R_{\rm tr}}\right)\right) \tag{4.1}$$

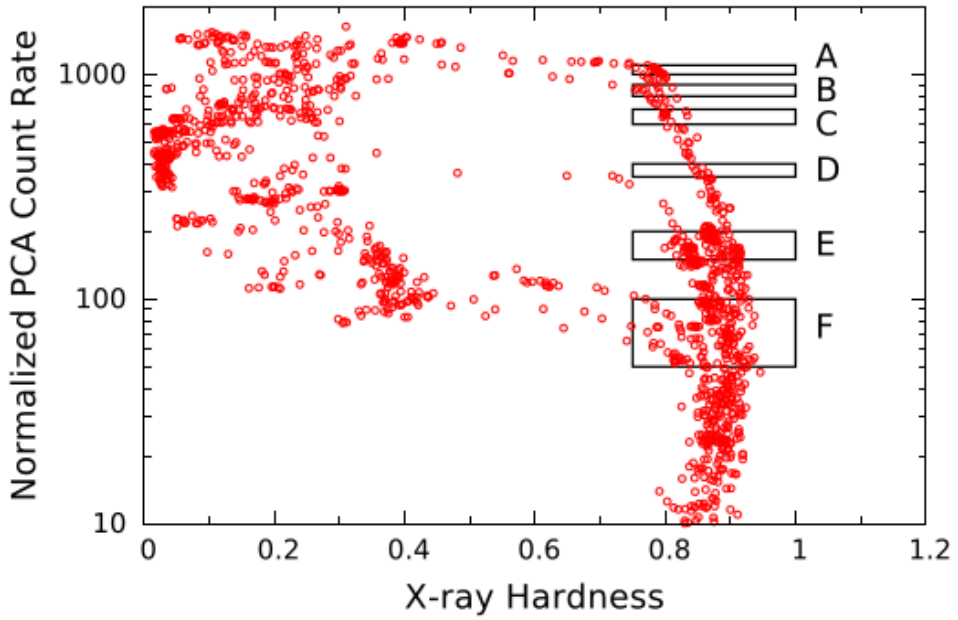

Figure 4.1: Hardness intensity diagram from GX 339-4 system. The vertical axis shows the count rate. On the horizontal axis is the hardness ratio HR defined as the ratio of source counts at 8.6–18 keV to the counts at 5–8.6 keV. Image taken from Garcia et al. (2015).

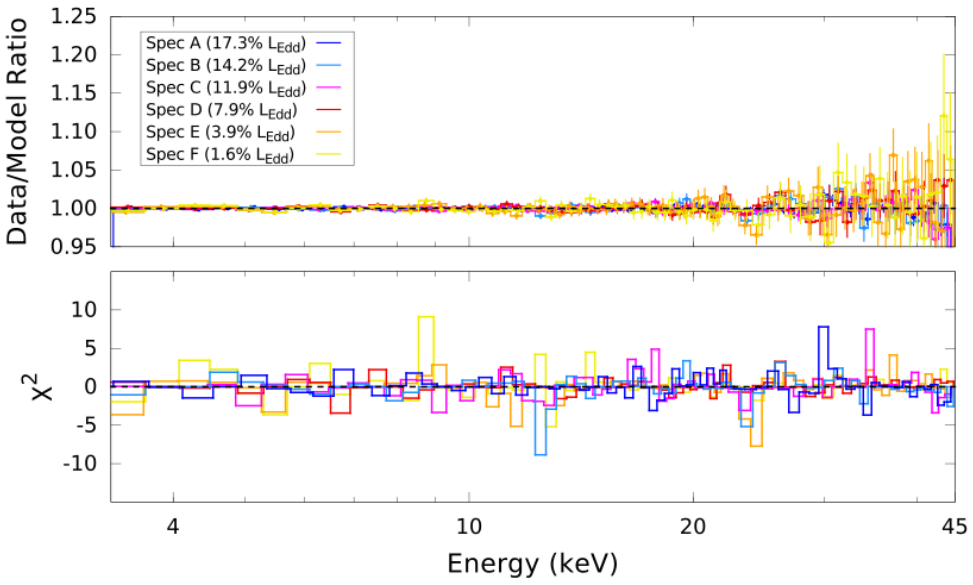

Figure 4.2: Fit to spectra A-F, where in the top image the ratio between the data and the canonical model 3 is plotted. The model produces an excellent fit, giving $\chi^2_{\rm red} = 1.06$. The bottom image shows the χ^2 for the model. Image taken from Garcia et al. (2015).

where

$$C(x) \equiv 3x^{-1} - 2x^{-3/2}, \tag{4.2}$$

$R_{\rm g}$ is the gravitational radius and $R_{\rm out}$ is the thin disk outer edge, which is fixed at an

arbitrarily large value, because the system has a large size and $C(x) \approx 0$ for $x \gg 1$ (Reb et al., 2018).

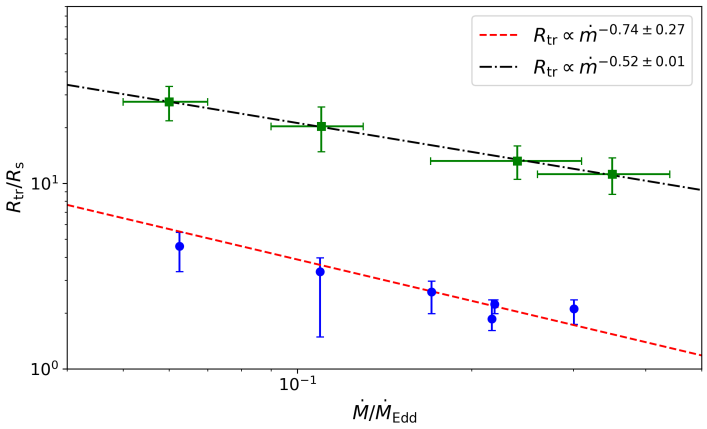

Figure 4.3: Comparison between the $R_{tr} - \dot{m}$ relation predicted by our model and observations. The green squares indicates the points from this work and the blue circles the data from Garcia et al. (2015). The red dashed line indicates the power law fit for the data from Garcia et al. (2015) (where $R_{tr}/R_s = 0.7\dot{m}^{0.74}$) and the black dot-dashed line the power law fit for this work (where $R_{tr}/R_s = 6.4\dot{m}^{0.51}$).

In Figure 4.3, it is possible to see that the overall dependency of r_{tr} on $\dot{m}$ found in this work is consistent with that found for GX 339-4 from Garcia et al. (2015) within 1σ uncertainties. The main difference between the results is that for a given $\dot{m}$, the predicted radii are systematically larger by a factor of four. As argued by Garcia et al. (2015), their estimates of the truncation radius seem to be the most accurate. One of the reasons is the development of a calibration tool which can improve the precision of the detector response by approximately one order of magnitude (check section 1.3 from Garcia et al., 2015). One should keep in mind that Garcia et al. (2015) may be underestimating the values of the truncation radius because of the lack of evidence for the thermal disk component in their modeling. It is also worth to note that previous estimates of the truncation radius have very high uncertainties (check table 5 of Garcia et al., 2015).

If the parameters obtained in Garcia et al. (2015) reflect the physical reality of the source, one possible explanation for the larger values of r_{tr} obtained in the present work could be the effect of a nonzero BH spin. For non-rotating BHs the ISCO (see section 1.2) is located at 6 gravitational radii. For a Kerr BH—which is the case for the system studied in Garcia et al. (2015)—the ISCO can extend all the way down to one gravitational radius for a_* close to 1. It is possible that r_{tr} might shift to lower values if the effects on the disk

of the Kerr spacetime were taken into account.

Another explanation could be the way the truncation radius was obtained here. If the assumption was that the truncation radius starts at the first time that the aspect ratio reached a value of < 0.015 (check Figure 3.7 and the explanation on how the truncation radius was obtained), the truncation radius would certainly be smaller, which would shift the power-law fit in Figure 3.9.

4.2 Comparison with other models

Our result is consistent with the expectation that the truncation radius should increase with decreasing accretion rate. However, the -1/2 slope is inconsistent with some earlier studies such as the evaporation model (Meyer and Meyer-Hofmeister, 1994; Liu et al., 1999) which predicts $-1/1.17$ and the turbulent diffusion model (Honma, 1996; Kato and Nakamura, 1998) where the predicted slope is -2. Both models will be briefly discussed in the next paragraphs.

For the evaporation model, the following physical mechanism is proposed. The coronal flow is dominated by heat conduction by electron and the thin disk is dominated by radiative cooling. But, in somewhere near the surface of the thin disk there is an equilibrium between them. If the system were in an stationary state, it would be in equilibrium, but the coronal flow is being accreted. Thus, because of the accretion the density of the equilibrium region gets smaller and then the heat conduction start dominating, meaning that the gas lost by the corona is resupplied by the evaporation of the surface of the thin disk (for more details on the evaporation model check: Meyer and Meyer-Hofmeister, 1994; Liu et al., 1999).

For the turbulent diffusion, Honma (1996) and Kato and Nakamura (1998) propose that the energy from the hot accretion flow is transported by means of diffusion through turbulence and by means of radial flow.

Liu et al. (1999) compared their analytical evaporation model with observations and they found it is consistent with the observation of three BHXB systems. However, as Garcia et al. (2015) shows in Figure 11, different models fitting observational data to estimate the truncation radius for the same object result in very different values compared to one another, spanning a range of values from ~ 1 to $\sim 10^3$ gravitational radii.

Regarding our result that the corona contracts in response to an increase in $\dot{m}$. There is much debate over whether the state transition from the hard to the soft state in BHBs is driven mainly by a reduction of the truncation radius of the disk (Ingram and Done, 2011) or by a reduction in the spatial extent of the corona (Fabian et al., 2014; Kara et al., 2019). In this work, both properties are affected by the increasing $\dot{m}$.

4.3 Caveats

In this section, the simplifications used in the simulations will be discussed.

4.3.1 Simplification in radiative cooling

The first simplification made was the use of the critical frequency ν_c of the self-absorbed synchrotron emission for the synchrotron cooling rate. It is also used as the seed photon frequency for the comptonized synchrotron. This was done to avoid the integration over frequencies thereby reducing the computational cost.

Another simplification is the fact that the comptonization is local, meaning that the photons do not propagate over long distances. Photons can interact with hot electrons very far away from where it was produced, but to account for this, the inclusion of a radiative transfer codes (applying Monte Carlo technique) would be necessary, which is very time-consuming.

4.3.2 Magnetic fields

This work consisted of hydrodynamic simulations in which there are no global magnetic fields. Instead, the plasma β parameter approximation was used assuming equipartition to estimate the magnetic field strength and thus compute the synchrotron emission.

The β parameter can only account for the local and randomly oriented (tangled) magnetic field. MHD simulations show that it is not constant as assumed here (e.g. Yuan and Narayan 2014). Meyer and Meyer-Hofmeister (2002) argues that with increasing magnetic field there is a reduction of the strength of the coronal mass flow if dynamo action occurs, meaning that, as inside of the truncation radius all matter is accreted in a hot corona form, the truncation radius would be shifted to smaller radii. But as shown in Figure 1 from Meyer and Meyer-Hofmeister (2002), the slope of the $R_{\rm tr}$-$\dot{m}$ relation will not change. This

dynamo effect could also be one of the explanations of the discrepancy for the truncation radius values in section 3.2.

4.3.3 α-viscosity

An α-viscosity prescription that is proportional to the density of the gas was assumed in this work. This means that most of the viscous heating is taking place at the equatorial plane of the accretion flow. But, MHD simulations considering magnetic reconnection as the physical heating mechanism, indicates that the vertical distribution of energy dissipation can extend to much higher heights (Jiang et al., 2014). If this is taken into account the equatorial plane would be cooler and the higher altitudes would be hotter.

Chapter 5

Conclusions

In this work, global numerical hydrodynamical simulations of black hole accretion flows were performed, incorporating the contribution of radiative cooling from bremmstrahlung, synchrotron and comptonized synchrotron to energy losses in a simplified way. The natural emergence of a thin disk embedded in a hot corona is observed in the simulations, whose inner radius is truncated at a range of radii from 11.2 to 27.5 Schwarzschild radii which are larger than the innermost stable circular orbit of $6GM/c^2$ for a Schwarzschild BH. The truncated, colder, denser thin disk is embedded in a hot, geometrically thick corona which is believed to be a RIAF.

Analysing the properties of the accretion flow in the simulations, the following radial dependency of the disk properties were found for the thin disk: $\rho \propto r^{-1.43}$, $v_{\rm r} \propto r^{-0.44}$, $T \propto r^{-0.71}$ and $v_\phi \sim v_{\rm K}$. These are in disagreement with the analytical predictions of the Shakura and Sunyaev (1973) disk. One possible reason for the mismatch are the simplifications imposed on the radiative cooling calculations which mainly affect the optically thick flow, and the opacity not being the Kramer's law.

For the RIAF, the following radial variation were found: $\rho \propto r^{-1.25}$, $v_{\rm r} \propto r^{-0.52}$, $T \propto r^{-0.95}$ and $v_\phi < v_{\rm K}$. They seem to be consistent with the results expected from analytical RIAF models (Narayan and Yi, 1995; Yuan and Narayan, 2014). Thus, even though the radiative cooling was treated in a simplified manner, this suggests it is a consistent approximation—at least for the optically thin flow.

When the accretion rate is above a critical value in the range $\dot{m}_{\rm crit} = 0.06 - 0.02$, a thin disk is observed to emerge. This would correspond to the thermal or soft state of BHBs. Below this critical value, the accretion flow remained very hot, low in density and geometrically thick and no thin disk is observed. This suggests that the accretion flow is

dominated by a RIAF, i.e. probably the very beginning of the hard state.

The models imply that the inner radius of the thin disk gets larger as $\dot{m}$ increases, following the power-law dependency $R_{\rm tr} \propto \dot{m}^{-\Gamma}$ where $\Gamma = 0.52 \pm 0.01$. The slope Γ found in this work is compatible with the results of Garcia et al. (2015) within uncertainties, where they studied the hard state of GX 339-4 in six different epochs.

Our inner radii are systematically larger by a factor of four than those obtained for GX 339-4. One possible explanation is that a Schwarzschild BH was modeled here whereas a spinning BH would be more appropriate depending on the source being modeled. Another possible explanation is Garcia et al. (2015) might be underestimating the values of the truncation radius, because they find no evidence for the thermal disk component.

The hot corona was found to decrease in size as $\dot{m}$ is increased. This result, together with the relation between the truncation radius and the accretion rate, favours the scenario where, in the hard state the disk is truncated at large radii (or entirely absent) and in the soft state there is a decrease in the illuminating source height (e.g. Plant et al. 2014; Garcia et al. 2015) together with a smaller inner radius.

Finally, another feature observed analysing the simulations was that the temperature decreases slightly as $\dot{m}$ increases. This was also found and shown in Table 6 of Garcia et al. (2015). This result is expected because of the radiative cooling, which makes the electron temperature to decrease, increasing the the energy transfer rate and finally decreasing the temperature of the ions.

5.1 Perspectives

The simulations of this work are purely hydrodynamical. Hence, a natural next step to move to magnetohydrodynamic (MHD) simulations which incorporate the effect of magnetic fields. The advantage of MHD simulations is that they self-consistently incorporate the angular momentum dissipation via the MRI mechanism. The disadvantage is that the computational costs will be considerably increased, especially for the thin disk when small-scale magnetic fields threading the disk will need to be resolved, requiring considerable numerical resolutions.

Another aspect to improve are the approximations of the radiative cooling. But this is actually very difficult to take into account as the more accurate techniques (e.g. Monte

Carlo) are very time consuming. Furthermore, radiation pressure gets increasingly important as $\dot{m}$ increases, and it is entirely neglected here. This certainly deserves further investigations.

As was argued when comparing the results of this work with the BHB GX 339-4, the Kerr spacetime is also relevant. This would require to use general relativistic MHD codes. Overall, GRRMHD (general relativistic radiation magnetohydrodynamic) codes would need to be adopted to properly describe the full regime of BH accretion. While the field of GRRMHD simulations is still young, this certainly remain a promising avenue of research for the future.

Finally, it is very important to compare the observational results with the numerical ones to obtain physical insights. Thus, it is hoped that more observational data will be available, so that it is possible to constrain the physical explanations of the truncation radius and its relation with the mass accretion rate. Also, plans are being made to generate synthetic electromagnetic spectra from our simulations that can be compared against BHB observations.

Bibliography

Abbott B. P., Abbott R., Abbott T. D., Abernathy M. R., Acernese F., Ackley K., Adams C., Adams T., Addesso P., Adhikari R. X., et al. Astrophysical Implications of the Binary Black Hole Merger GW150914, ApJ, 2016, vol. 818, p. L22

Abramowicz M. A., Czerny B., Lasota J. P., Szuszkiewicz E., Slim Accretion Disks., Apj, 1998, vol. 332, p. 646

Antonucci R., Thermal and Nonthermal Radio Galaxies., Astronom Astrophys Transactions, 2012, vol. 27, p. 557

Balbus S. A., Hawley J. F., Instability, turbulence, and enhanced transport in accretion disks, Reviews of Modern Physics, 1998, vol. 70, p. 1

Batten P., Clarke N., Lambert C., Causon D. M., On the Choice of Wavespeeds for the HLLC Riemann Solver., SIAM Journal on Scientific Computing, 1997, vol. 18, p. 1553

Blandford R. D., Begelman M. C., On the fate of gas accreting at a low rate on to a black hole, Monthly Notices of the Royal Astronomical Society, 1999, vol. 303, p. L1

Bowyer S., Byram E. T., Chubb T. A., Friedman H., Cosmic X-ray Sources., Science, 1965, vol. 147, p. 394

Cattaneo A., Fabe S. M., Binney J., et al. The role of black holes in galaxy formation and evolution., Nature Review, 2009, p. 22

Das U., Sharma P., Radiatively inefficient accretion flow simulations with cooling: implications for black hole transients, Monthly Notices of the Royal Astronomical Society, 2013, vol. 435, p. 2431

Dermer C. D., Liang E. P., Canfield E., Luminosity enhancement factor for thermal Comptonization and the electron energy balance, The Astrophysical Journal, 1991, vol. 369, p. 410

Done C., Scaling accretion flow models from BHB to AGN., in Suzaku-MAXI 2014: Expanding the Frontiers of the X-ray Universe, 2014, p. 300

Esin A. A., McClintock J. E., Narayan R., Advection-Dominated Accretion and the Spectral States of Black Hole X-Ray Binaries: Application to Nova Muscae 1991, The Astrophysical Journal, 1997, vol. 489, p. 865

Fabian A. C., Parker M. L., Wilkins D. R., Miller J. M., Kara E., Reynolds C. S., Dauser T., On the determination of the spin and disc truncation of accreting black holes using X-ray reflection, Monthly Notices of the Royal Astronomical Society, 2014, vol. 439, p. 2307–2313

Fender R., Belloni T., Stellar-Mass Black Holes and Ultraluminous X-ray Sources, Science, 2012, vol. 337, p. 540

Frank J., King A., Raine D., Accretion power in astrophysics. Cambridge university press, 2002

Frolov V., Novikov I., Black Hole Physics. Springer Netherlands, 1998

Garcia J. A., Steiner J. F., McClintock J. E., Remillard R. A., Grinberg V., Dauser T., X-ray reflecction spectroscopy of the black hole GX 339-4: Exploring the hard state with unprecedented sensitivity., The Astrophysical Journal, 2015, vol. 813, p. 84

Glowinski R., Osher S. J., Yin W., Splitting Methods in Communication, Imaging, Science, and Engineering. Springer, Cham, 2016

Greene J., Strader J., Ho L., Intermediate-Mass Black Holes, 2019, p. 70

Hartle J. B., Gravity : An Introduction to Einstein's General Relativity. California: Addison-Wesley, 2003

Ho L. C., Nuclear Activity in Nearby Galaxies., Annual Review of Astronomy and Astrophysics, 2008, vol. 46, p. 475

Honma F., Global Structure of Bimodal Accretion Disks around a Black Hole, PASJ, 1996, vol. 48, p. 77

Hubeny I., Vertical structure of accretion disks - A simplified analytical model, The Astrophysical Journal, 1990, vol. 351, p. 632

Ingram A., Done C., A physical model for the continuum variability and quasi-periodic oscillation in accreting black holes, Monthly Notices of the Royal Astronomical Society, 2011, vol. 415, p. 2323–2335

Jiang Y. F., Stone J. M., Davis S. D., Radiation magneto-hydrodynamic simulations of the formation of the hot accretion disk coronae., Apj, 2014, vol. 784, p. 169

Kara E., Steiner J. F., Fabian A. C., Cackett E. M., Uttley P., Remillard R. A., Gendreau K. C., Arzoumanian Z., Altamirano D., Eikenberry S., Enoto T., Homan J., Neilsen J., Stevens A. L., The corona contracts in a black-hole transient, Nature, 2019, vol. 565, p. 198

Kato S., Nakamura K. E., Transition Radius from Cooling-Dominated to Advection-Dominated Regimes in Two Temperature Disks, PASJ, 1998, vol. 50, p. 559

Liu B. F., Yuan W., Meyer F., Meyer-Hofmeister E., Xie G. Z., Evaporation of accretion disks around black holes: The disk-corona transit, The Astrophysical Journal, 1999, vol. 527, p. L17

McClintock J. E., Remillard R. A., In compact stellar X-ray sources, Cambridge Astrophysics Series, 2009, vol. 39, p. 157

McKinney J. C., Tchekhovskoy A., Sadowski A., Narayan R., Three-dimensional general relativistic radiation magnetohydrodynamical simulation of super-Eddington accretion, using a new code HARMRAD with M1 closure., Monthly Notices of the Royal Astronomical Society, 2014, vol. 441, p. 3177–3208

Meier D. L., Black Hole Astrophysics: The Engine Paradigm, Springer, Verlag Berlin Heidelberg, 2012

Merloni A., Heinz S., di Matteo T., A Fundamental Plane of black hole activity., Monthly Notices of the Royal Astronomical Society, 2003, vol. 345, p. 1057

Meyer F., Meyer-Hofmeister E., Accretion disk evaporation by a coronal siphon flow, Astronomy and Astrophysics, 1994, vol. 288, p. 175

Meyer F., Meyer-Hofmeister E., The effect of disk magnetic fields on the truncation of geometrically thin disks in AGN., A&A, 2002, vol. 392, p. L5

Mignone A., Bodo G., Massaglia S., Matsakos T., Tesileanu O., Zanni C., Ferrari A., PLUTO: a numerical code for computational astrophysics, The Astrophysical Journal Supplement Series, 2007, p. 228

Narayan R., Mahadevan R., Quataert E., Advection-Dominated Accretion around Black Holes., To appear in The Theory of Black Hole Accretion Discs, eds. M. A. Abramowicz, G. Bjornsson, & J. E. Pringle (Cambridge University Press), 1998

Narayan R., Sadowski A., Penna R. F., Kulkarni A. K., GRMHD simulations of magnetized advection-dominated accretion on a non-spinning black hole: role of outflows., Monthly Notices of the Royal Astronomical Society, 2012, vol. 426, p. 3241

Narayan R., Yi I., Advection-dominated Accretion: Underfed Black Holes and Neutron Stars, The Astrophysical Journal, 1995, vol. 452, p. 710

Nemmen R. S., Brotherton M. S., Quasar bolometric corrections: theoretical considerations., Monthly Notices of the Royal Astronomical Society, 2010, vol. 438, p. 2804

Nemmen R. S., Georganopoulos M., Guiriec S., Meyer E. T., Gehrels N., Sambruna R. M., A Universal Scaling for the Energetics of Relativistic Jets from Black Hole Systems, Science, 2012, vol. 338, p. 1445

Nemmen R. S., Storchi-Bergmann T., Eracleous M., Spectral models for low-luminosity active galactic nuclei in LINERs: the role of advection-dominated accretion and jets, Monthly Notices of the Royal Astronomical Society, 2014, pp 2804–2827

Newman E. T., Couch E., Chinnapared K., Exton A., Prakash A., Torrence R., Metric of a rotating, charged mass, Journal of mathematical physics, 1965, vol. 6, p. 918

Ozel F., Psaltis D., Narayan R., Villarreal A. S., On the mass distribution and birth masses of neutron stars., Apj, 2012, vol. 757

Pacholczyk A. G., Radio astrophysics. Nonthermal processes in galactic and extragalactic sources. San Francisco: Freeman, 1970

Paczynsky B., Wiita P. J., Thick accretion disks and supercritical luminosities, Astronomy and Astrophysics, 1980, vol. 88, p. 23

Papaloizou J., Pringle J., The dynamical stability of differentially rotating discs with constant specific angular momentum, Monthly Notices of the Royal Astronomical Society, 1984, vol. 208, p. 721

Piran T., Sadowski A., Tchekhovskoy A., Jet and disc luminosities in tidal disruption events., Monthly Notices of the Royal Astronomical Society, 2015, vol. 453, p. 157

Plant D. S., Fender R. P., Ponti G., Muñoz-Darias T., Coriat M., Revealing accretion onto black holes: X-ray reflection throughout three outbursts of GX 339−4, Monthly Notices of the Royal Astronomical Society, 2014, vol. 442, p. 1767–1785

Porth O., Chatterjee K., Narayan R., et al. The Event Horizon General Relativistic Magnetohydrodynamic Code Comparison Project., The Astrophysical Journal Supplement Series, 2019, vol. 243

Reb L., Fernández-Ontiveros J. A., Prieto M. A., Dolag K., A lower limit to the accretion disc radius in the low-luminosity AGN NGC 1052 derived from high-angular resolution data., Monthly Notices of the Royal Astronomical Society, 2018, vol. 478, p. L122

Remillard R. A., McClintock J. E., X-Ray Properties of Black-Hole Binaries, Annual Review of Astronomy & Astrophysics, 2006, vol. 44, p. 49

Ryan B. R., Dolence J. C., Gammie C. F., bhlight: General Relativistic Radiation Magnetohydrodynamics with Monte Carlo Transport., The Astrophysical Journal, 2015, vol. 807, p. 58

Sadowski A., Narayan R., McKinney J. C., Tchekhovskoy A., Numerical simulations of super-critical black hole accretion flows in general relativity., Monthly Notices of the Royal Astronomical Society, 2014, vol. 439, p. 503–520

Shakura N. I., Sunyaev R. A., Black holes in binary systems. Observational appearance., Astronomy and Astrophysics, 1973, vol. 24, p. 337

Stepney S., Guilbert P. W., Numerical fits to important rates in high temperature astrophysical plasmas, Monthly Notices of the Royal Astronomical Society, 1983, vol. 204, p. 1269

Stone J. M., Pringle J. E., Magnetohydrodynamical non-radiative accretion flows in two dimensions., Monthly Notices of the Royal Astronomical Society, 2001, vol. 322, p. 461

Stone J. M., Pringle J. E., Begelman M. C., Hydrodynamical non-radiative accretion flows in two dimensions, Monthly Notices of the Royal Astronomical Society, 1999, vol. 310, p. 1002

Toro E. F., Riemann solvers and numerical methods for fluid dynamics: a practical introduction. Springer Science & Business Media, 2013

Toro E. F., Spruce M., Speares W., Restoration of the contact surface in the HLL-Riemann solver. Springer-Verlag, 1994

Vogelsberger M., Genel S., Springel V., Torrey P., Sijacki D., Xu D., Snyder G., Bird S., Nelson D., Hernquist L., Properties of galaxies reproduced by a hydrodynamic simulation., Nature, 2014, vol. 509, p. 177–182

Wu M.-C., Xie F-G Yuan Y.-F., Gan Z., Hot accretion flow with radiative cooling: state transitions in black hole X-ray binaries, Monthly Notices of the Royal Astronomical Society, 2016, vol. 459, p. 1543

Xie F., Yuan F., Radiative efficiency of hot accretion flows., Monthly Notices of the Royal Astronomical Society, 2012, vol. 427, p. 1580–1586

Yuan F., Bu D., Wu M., Numerical simulation of hot accretion flows. II. Nature, origin, and properties of outflows and their possible observational applications, The Astrophysical Journal, 2012, vol. 761, p. 130

Yuan F., Cui W., Narayan R., An accretion-jet model for black hole binaries: interpreting the spectral and timing features of XTE J1118+480., Apj, 2005, vol. 620, p. 905

Yuan F., Narayan R., Hot accretion flows around black holes, Annual Review of Astronomy and Astrophysics, 2014, vol. 52, p. 529

Appendix

Appendix A

Computational infrastructure

A.1 Codes

The main code used for the simulations was the `PLUTO` code by Mignone et al. (2007). A general description of this code was given in Section 2.2.

Besides `PLUTO`, some scripts were written to analyse the data and to compute the radiative cooling. The main script written by some members of the group to analyse and visualize `PLUTO`'s output is called `mickey`. This code was written mainly in python language with some `C` routines to make regridding faster. The script to compute the table with the values of radiative cooling for a combination of the variables T_e, n_e and R was written by the author of this work. This script was written in python and is called `radiative_cooling`.

A.2 Clusters

Below, in the subsections, the clusters used in this work to compute the numerical simulation will be briefly described.

A.2.1 Águia

The Águia cluster is constituted by 128 physical servers with 20 cores and 512 GB of RAM. The processor is the Intel(R) Xeon(R) CPU E7- 2870 @ 2.40GHz. The cluster also has a Filesystem with 256 TB for temporary files.

A.2.2 Santos Dumont

The Santos Dumont cluster is located in Laboratório Nacional de Computação Científica (LNCC). It has a processing capacity of 5.1 Petaflop/s and a total of 34688 CPU cores in 1132 computational nodes. Besides that, there is also a special node projected to Artificial Intelligence applications with 8 GPUs NVIDIA Tesla V100-16Gb with Nvlink.